8-2009

Finite Element Modeling of Fluid Flow and Heat Transfer in the Weld Pool of CMSX-4 Nickel Based Superalloy

Jeremy Payne
Lehigh University

Finite Element Modeling of Fluid Flow and Heat Transfer in the Weld Pool of CMSX-4 Nickel Based Superalloy

Jeremy Payne

A Thesis

Presented to the Graduate and Research Committee of

Lehigh University

In Candidacy for the Degree of

Master of Science

Mechanical Engineering and Mechanics

Lehigh University

Bethlehem, PA

August, 2009

LEHIGH UNIVERSITY

Bethlehem, Pennsylvania

_____

This Thesis is accepted and approved in partial fulfillment of the requirements for the Master of Science

_____

Herman F. Nied, Ph.D.,
Thesis Advisor

_____

D. Gary Harlow, Ph.D.,
Chair, Mechanical Engineering and Mechanics

_____

Date

Acknowledgements

I would like to thank Professor Herman Nied for his insight and support during this project. His guidance made it possible to push through to accomplish the goals.

I would also like to thank Professor John DuPont for his additional support and information in the Material Science field that helped to add a great element to the project.

Next, I would like to thank the Department of Mechanical Engineering for the financial support during my studies. Without this support I would have not been able to continue on with my education to this point.

Finally, I need to thank my family members and close friends who have been with me through my educational endeavors. Without their love and support this journey would have been far too difficult.

Table of Contents

Abstract

The goal of this study is to determine the characteristics necessary to develop a robust finite element model to accurately predict weld pool shape, size, and fluid properties during a repair weld to a piece of CMSX-4 Nickel-based superalloy. The calculations will take into account the possibilities of turbulence, temperature dependent material property values and different heat input values. It is expected that the model created using the FIDAP software package from FLUENT will be beneficial for future welding simulations. This model was also compared to results from a FORTRAN code written by a separate group at Penn State that have previously been found to be comparable to acceptable experimental values.

Introduction

The growing concern for energy sources capable of higher output values and efficiency rates has led to advancements in materials as well as equipment designs. These designs include improved turbine blade engines such as those used for aerospace applications and Industrial Gas Turbines (IGT) [1, 3]. In order to develop this higher production equipment, special concerns were made for the extreme conditions that would be experienced within the energy processes. By making the equipment run faster and hotter, the fuel sources are used at much more efficient rates. To do so, materials had to be chosen that could withstand these environments. One such common material is single crystal (SX) Nickel-based Superalloys [1, 3-6]. These special alloys are used for their superior resistance to thermo-mechanical loads that would usually cause creep and other high temperature degradation failures. Unfortunately, this comes at a very high production cost (around $30,000 per blade [2]) and the blades will still have failure at some point in their lifetimes. Power plants can lose upwards of hundreds of thousands of dollars in revenue during failure induced downtime. Therefore, it is highly desirable to keep the equipment in good operating condition as well as the ability to repair failed parts in a timely fashion.

There are many scenarios that are detrimental to the lifespan of machinery such as high temperature hot corrosion (Type-I corrosion) [4-5], foreign object damage (FOD) [7], and creep as well as cracking caused by fatigue in the high temperature environments [6]. Although, as said earlier, the SX Ni-based Superalloys have high resistances to extreme temperatures, creep failures and other thermo-mechanical loads, they do not have a very high corrosion resistance. In order to accommodate this, simple coatings of other materials, such as aluminum or platinum [4], which have high corrosion resistance, are used. Eventually, as the number of cycles increases, the corrosion resistant coatings deteriorate as a result of high cycle fatigue (HCF) or as a result of a flaw in the surrounding machinery, i.e. clearance issues that would cause wear [5]. Once the coatings begin to wear off, the high temperature gases that are flowing through the turbine begin to eat away at the exposed areas by way of the Type-I corrosion. Once the corrosion starts, which is usually around the tip of the blade, cracks begin to form along the length of the blade and hence shortening the service life of the blade. It was found in

[5] that cracks did not occur far away from the wear area, thereby pinpointing the main root cause of the failure to the uneven clearance that the rotating turbine blades experienced. Another study [4] examined the failure of the corrosion resistant coating due to thermo-mechanical failures. As stated previously, many coatings are made from aluminum, which has a brittle-to-ductile transition (300-500°C) much lower than the operating temperatures which are thought to be present (upwards of 1100°C). While the platinum modified coatings have slightly higher brittle-to-ductile transition temperatures, they will still experience some early signs of cracking, which will lead to the same type of failure as the previous example. A related failure mode occurs as a result of overheating where the operating temperatures are much higher than the designed specifications. This situation could arise due to improper filtering of cooling air which could be caused by clogs or damaged exit ports that would trap heat in the engine more than usual [6]. This type of scenario usually gives way to coupled failures, i.e. creep and fatigue that lead to cracks. This can be determined by examining the microstructure of the blade and noting the distinct transition points that give evidence of the phase changes that go along with those varying temperatures.

Another cause of failure, which occurs mostly in the aerospace turbines sector, is foreign object damage (FOD). Since the immense amount of airflow is entering the engine at a very high rate due to the suction effect of the rotating blades, smaller objects in the surrounding area often get pulled in. These foreign objects included ice and animals, considered soft body impact, as well as hard body objects which include rocks and metallic debris [7]. This damage often creates a notch or dent on the leading edge of the blades which creates a starting point for a crack to propagate. The study modeled this behavior by firing objects at the leading edge of a stationary blade and then the fatigue strength was tested and compared to theoretical results. One result of the study was that the predictive results actually created a lower bound to the experimental results in terms of the fatigue strength. This was thought to be attributed to the lack of ability to examine and model the residual stresses located near the crack tip. Another expected result was found in that the angle of impact, as well as the geometry of the initial damaged area, has a large influence on the affected fatigue life.

Once the damage is done, the next logical step is to attempt to repair it instead of

replacing the extremely high cost item. One must be careful in this situation as well so as not to limit the service life even more with the repair. This situation can occur in heat treatment during the refurbishment process [8]. Heat treatment is performed in hopes of returning the damaged unit to its original microstructure and subsequently its original properties. Heat treatment is also performed in order to relieve residual stresses in the work piece. All damages are different and therefore call for slightly different repair techniques, but this study proposes the hope for a general heat treatment process that would accomplish the previously stated goal. The study examined a refurbished blade that only performed for 900h of service compared to the 40,000h that the original model haled. An analysis of the microstructure and phases present showed that the blade was exposed to overheating as discussed earlier. Voids in the γ' phase showed the heat treatment was performed in an unacceptable manner which resulted in the quick failure of the blade.

Welding Techniques

In recent years, welding has gained increased interest in regards to cost saving processes. Although it has been found to account for approximately 20% of maintenance costs [2], it is far cheaper than the cost of new construction. There are many variations of welding but they can be categorized into two main types: Fusion and Nonfusion welding [40]. There are several subcategories under these main headings. First, fusion welding is defined as a process that requires intense amounts of heat in order to melt the materials which allows the bonds between the work pieces to form. When melting is not present or is not the primary driving force behind the joining, then the process is considered to be a nonfusion one. These nonfusion processes usually employ high pressure in order to create the bond between pieces. Examples of nonfusion include friction welding where materials are under extreme pressures in order to keep them in contact while they move against each other, which causes friction to build and heat up the pieces and diffusion welding (DFW) which is "a solid-state welding process that produces a weld by the application of pressure at elevated temperatures with no macroscopic deformation or relative motion of the work pieces" [40]. These processes are not as common as their fusion brethren.

Fusion welding can be broken down into a few subcategories: Chemical Fusion, Electric Arc, and High Energy Intensity welding. Chemical Fusion processes include high temperature flames acting on the surface in order to induce melting. An example would be Oxyfuel Gas Welding. Next, a much more common technique is Electric Arc Welding which can be broken down into consumable and non-consumable electrode processes. Arc welding techniques require shielding from atmospheric disturbances. This is accomplished by either an inert gas creating a shroud of sorts around the arc or by the usage of flux that will also create a cover while it helps to clean and remove impurities in the weld. The non-consumable variety includes Gas Tungsten Arc Welding (GTAW), which is also known as Tungsten Inert Gas (TIG) Welding which employs a non-consumable tungsten rod in order to act as an electrode that creates an arc which heats the metal to produce the weld [11]. A similar method to GTAW is Plasma Arc Welding (PAW) which also employs a non-consumable tungsten electrode. The difference is that the electrode in GTAW extends out of the nozzle, while the PAW

electrode is kept in the nozzle and a shielding gas surrounds the arc to keep it more concentrated than GTAW [40]. This difference can be seen in Figure 1 below. In both techniques a filler metal is sometimes used in order to complete the weld. Therefore the skill level required is increased since the welder must control all the parameters involved in keep the arc properties constant, as well as inserting the filler metal into the pool. Note that this filler metal is not always required.

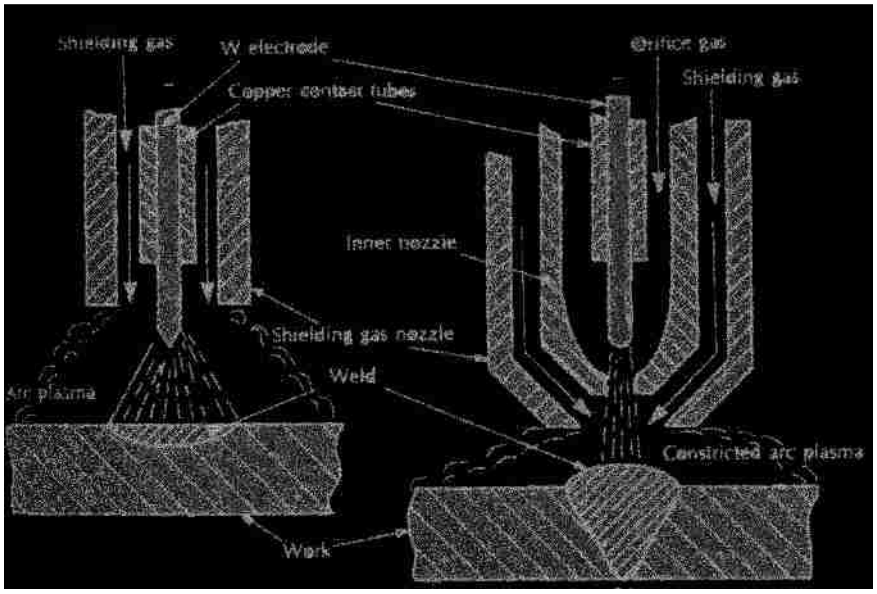

Figure 1 – Side by Side Comparison of GTAW (left) and PAW (right) from [40]

In the consumable electrode realm there are many different processes that accomplish the same basic task. As stated previously, welding techniques often require a filler metal. With the consumable electrode, the filler metal also serves as the electrode. Therefore as the metal droplets leave the tip, more is fed into the apparatus in order to keep the arc length constant. The first process included in this type is Gas Metal Arc Welding (GMAW), also commonly referred to as stick welding, which uses consumable rods that are covered in flux. This technique is good for quick repairs, but it is not a preferred method in production as the rods must be replaced which results in discontinuity. Shielded Metal Arc Welding (SMAW) and Flux Cored Arc Welding (FCAW) both use flux infused wires that are continuously fed into the system. The main difference is that SMAW has the flux on the outside similar to GMAW whereas FCAW, as the name would suggest, has the flux in the core of the wire. A final example of a consumable electrode process is Submerged Arc Welding (SAW) which uses granular flux that is piled onto the

area to be welded while the consumable electrode is “submerged” into the pile [11, 40]. In the welding techniques that employ the use of an arc, the effects of electrical and magnetic forces are a hot topic in the determination of the laminar/turbulent modeling [35-37]. This subject will be discussed further in a later section.

The final form of fusion welding that will be looked at is the High Energy Intensity welding. This subcategory contains Electron Beam (EB) Welding and Laser Beam Welding (LBW). Electron Beam welding is performed by concentrating a beam of high velocity electrons through magnetic coils onto the surface of the work piece. There are different varieties of EB welding based upon the amount of vacuum that is used in the surrounding work space [11]. The amount of vacuum dictates the distance from the surface at which the beam can be discharged from. The vacuum acts as a shielding gas similar to that employed in arc welding techniques. It accomplishes this task by allowing the electrons to flow to the work piece without any impedance by other molecules or gases that may be present under natural atmospheric conditions. The most common application uses a high vacuum (order of 10^{-3} to 10^{-5} atm) [40] chamber where the entire work piece is placed into it. This allows for a very high efficiency rate since there is no interference and the issue of reflectivity is not a high concern with electrons as it is with photons in laser welding. Transfer efficiency with this type of EB welding is in the 90% range [40]. Other types of EB welding do not employ such high vacuum values such as a technique that uses no vacuum. Since atmospheric debris is still a concern, the distance between the gun, where the electrons exit, and work piece can only be a matter of centimeters. A more extreme solution to not having a vacuum is to accelerate the electrons to an incredible rate approaching the speed of light. By employing millions of volts, the beam would theoretically remain incredibly concentrated thereby avoiding interaction with other gases in the atmosphere. A more realistic approach is a technique called “soft” vacuum. This is similar to the chamber principle but the vacuum is produced at a lower level (10-1 to 10-2 atm) [40]. Finally a technique called Sliding-Seal Electron Beam (SSEB) can be used to produce a vacuum. The base of the chamber in the SSEB case is the work piece itself. This allows for greater mobility than larger chambers that house the entire work piece.

As the name would suggest laser welding employs a high powered laser to

accomplish essentially the same task as the EB welding method. Instead of using the kinetic energy of accelerating electrons, laser welding uses photons that come from light radiation. These photons come by way of a laser which is actually an acronym for Light Amplification Stimulated by Emission of Radiation [40]. The main issue with using photons instead of the electrons though is that certain materials will reflect the photons, thereby decreasing the efficiency of the process. Similar to EB welding, laser welding also needs some protection from the atmosphere in order to operate correctly. Instead of just a vacuum, laser welding employs an inert gas similar to some arc processes. Argon is often a common choice in order to fill a chamber that resembles the EB variety. There are two main types of lasers that are used: CO_2, which is an example of a gas laser, and Nd:YAG (neodymium-doped yttrium aluminum garnet), which is an example of a solid-state laser. In [10] a chapter is devoted to explanations and comparisons of the advantages and disadvantages of using each type of laser. While CO_2 lasers have very high electrical efficiencies and low operating costs, Nd:YAG counterparts are better for metals with reflectivity issues and can produce more heat than CO_2 lasers at the same power level inputs. It is also noted that this increased productivity allows the Nd:YAG laser to travel at much faster speeds and still reach the same depths. Another way to classify different laser welding techniques is by looking at the filler material used, if at all. Some techniques employ a ribbon or string of metal while others use powdered metal deposition in order to fill or build.

In [40] a comparison between the two High Energy Intensity processes is made. While both are very expensive and require very tight tolerances for fitting of the joints, the main difference comes through while comparing efficiencies. As stated earlier, reflectivity is an issue with the photons involved in laser welding, thus a drastic difference in electrical efficiency (the power into the system versus the power out, not necessarily the amount of power absorbed by the work piece) with EB welds close to 99% and laser welds around 12%. This also can come into play when considering the depth of the welds that are possible with each process. EB welds can always penetrate deep, while too much of the photon energy may be reflected away when working with certain materials, thereby resulting in a much more shallow weld. A final difference, that could be more of an occupational concern, is that EB welding generates x-ray radiation

while laser welding does not. This is important to keep in mind for the operators in industries that employ these techniques.

One of the major differences between the arc and high density methods is the area that is affected by the process or the Heat Affected Zone (HAZ). This area is not directly in contact with the heat source itself, but heat transferred from the weld pool gives way to changes in the surrounding material. Since metals are such good conductors, it has been found that the maximum value for melting efficiency, which is the ratio of the amount energy that is used for melting to the amount of energy that reaches the work piece [11]. Laser and EB welds produce the smallest HAZs due to their precision and dimensions while GTAW and other similar techniques have much larger ones. Therefore, this has direct implications on the tolerances that are allowable during the procedures. The tolerance of the joints was mentioned already above when comparing the High Energy Intensity processes as it is often possible to join pieces without the assistance of a filler metal. These tolerances often lead to these processes being fully automated while arc techniques have more leniencies which allows for human error. In the HAZ, the temperatures are at elevated levels but still below the liquidus temperature. This can be high enough to still affect certain properties as well as the microstructure of the material [11]. This idea will be discussed in greater detail later on as we examine the material science aspect of the HAZ and weld pool.

In certain instances, such as a dilute nickel alloy, GTAW techniques can be employed. However, with SX Superalloys, which have been discussed thus far, different methods, such as laser powder deposition, like the LENS process (which will be discussed in greater detail later), are necessary in order to maintain the physical characteristics of the original part. These alloys, such as CMSX-4, are very difficult to work with since the high alloyed nature and grain boundaries are vital to the material properties [3]. Thus, more precise welding techniques that have minimum HAZs are required. An interesting aspect is what two separate studies referred to as weldability, or what range defects are not expected [3, 9]. In order to avoid what they call the three main types of cracking and defects: 1) solidification cracking which is caused by a wide solidification range for the alloy, 2) grain boundary liquation cracking which occurs in the HAZ due to the local dissolution of grain boundary phases, and 3) strain age cracking, which is due to the

residual stresses that often form during post-weld treatments or high temperature service, they have developed a numerical method in order to predict the weldability of a material by selecting the appropriate parameters. The main topics of discussion are the welding speed and effective power, which is the actual amount of power delivered to the surface by the torch.

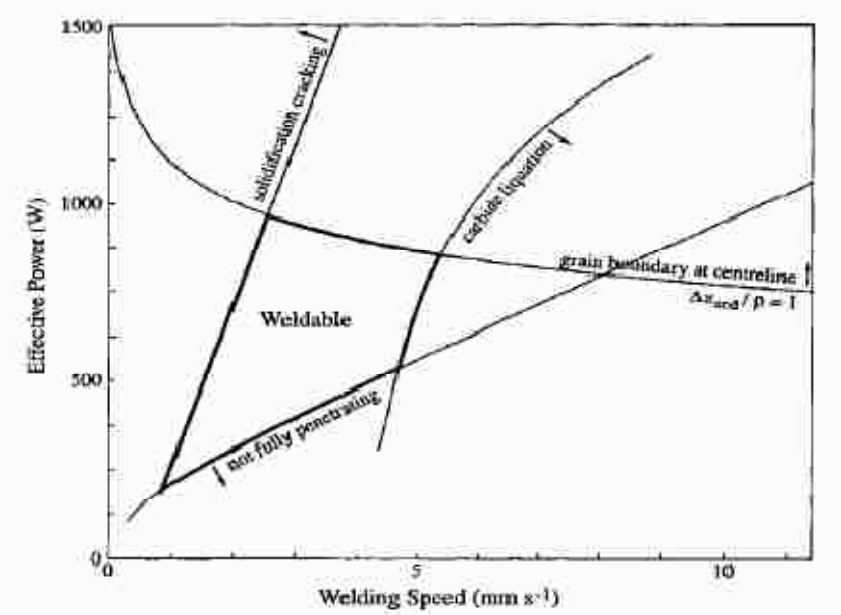

Figure 2 – Example of a weldability map for IN718 from [9]

Figure 1 shows the region for an Inconel Nickel-based alloy where the parameters are optimized in order to avoid certain defects. These plots take into account a Gaussian distribution of power on the surface, material conduction that allows for deeper penetration, and phase diagrams that examine the particle sizes that develop as a result of time and temperature. As noted, in the previous statement, the maps look at items that will depend very much on the chemical composition of the alloy.

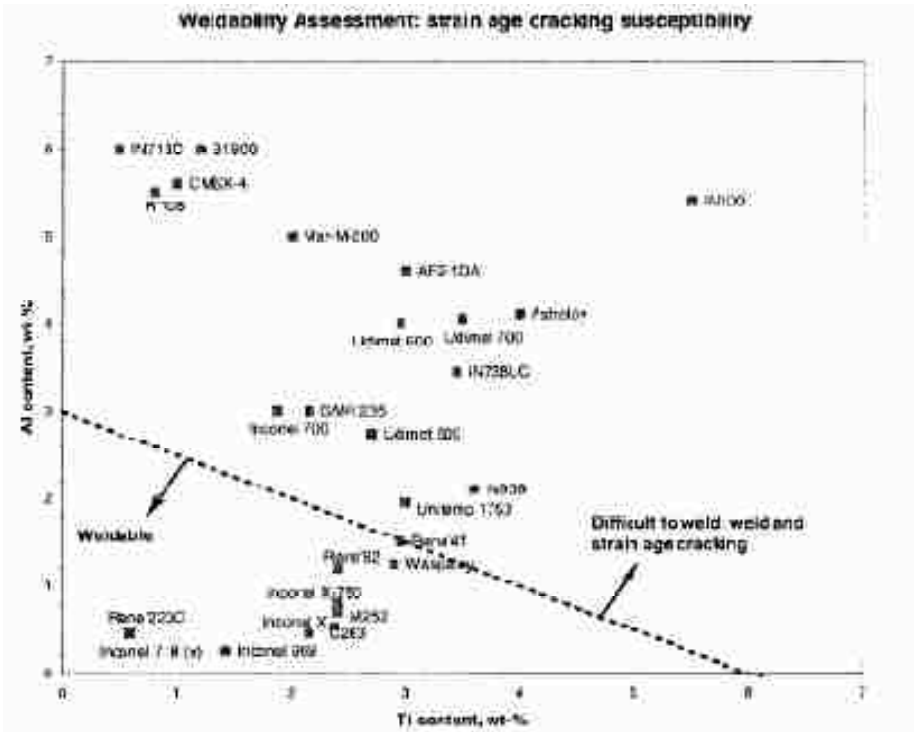

Figure 3 – Nickel Based Superalloy Weldability Based on Composition from [3]

Henderson et al. [3] examined the composition of nickel based alloys and arrived at the conclusion that there is a critical value for the level of aluminum and titanium that classifies a nickel based superalloy as easy or difficult to weld. Figure 2 shows that the weldability region has a linear cutoff value that corresponds to Al + Ti/2 = 3. It is of interest to note that the alloy that will be discussed almost exclusively for the duration of this work, CMSX-4, is far above the line in the difficult to weld region. This alloy is an ultra high strength, single crystal alloy developed by the Cannon Muskegon Corporation [33]. Since this material has a single crystal structure, [3] suggests that a laser welding process called Laser Metal Forming (LMF) Technology be employed. LMF uses a powder or wire material to deposit on the surface of the substrate, which in the case of a repair would be the blade itself. A similar method, which will be the main focus of the remainder of the paper, is the Laser Engineered Net Shaping (LENS) process that was developed by Sandia National Laboratory [12] and then later commercialized by Optomec. This process involves a laser that can move axially in the vertical direction and a platform that holds the substrate which has lateral and longitudinal movement in the perpendicular plane. A CAD file can be imported which is then divided into many layers.

These layers correspond to passes that the laser will make. During each pass, there are nozzles that introduce powdered metal into the area heated by the laser. This allows for the material to build up in a vertical fashion, thereby giving way to rapid prototyping or in the current case, the ability to repair machinery components.

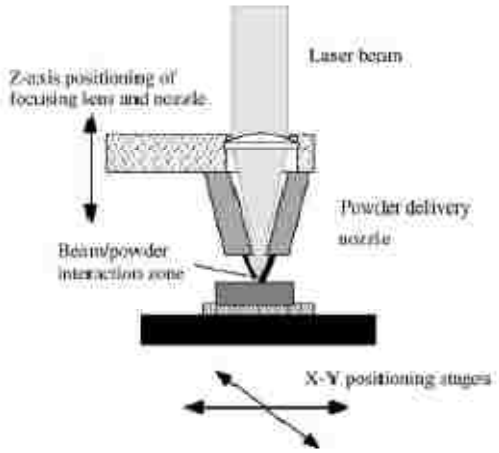

Figure 4 – Schematic of LENS Process [18]

There are many parameters that go into this process including the velocity at which the platform moves, the mass flow rate of the metal powder through the nozzles, which can be specified such that a gradient of material is possible, and the input power of the laser. Sensors are in place that monitor the size of melt pool and make small adjustments in order to maintain a consistent geometry. Note, that as in other processes, the LENS could also be used to produce autogenous welds where no filler metal is used.

Modeling Options

In recent years, it has become of increased interest to find the optimized welding input parameters of velocity and power by modeling the process and analyzing the results. Many different modeling techniques have been used including commercial codes [13-17], numerical analysis [9,18-19], and others which look at the heat source type and basic equations of heat transfer [17,21-23]. Since most of the other methods are based on the choices of the heat source model type, it is pertinent to discuss this first. Starting with the most simple and becoming more complex in nature, the first type of model is a 1-D moving heat front [23]. This model is a simple one where a temperature or heat flux is imposed along a moving heat front at a constant velocity. Governing equations for this model are based on a source and sink approach to heat transfer. Using Fourier's Law and arriving at:

$$-k\left[\frac{\partial T(Vt^{+},t)}{\partial x}-\frac{\partial T(Vt^{-},t)}{\partial x}\right]=q^{+}+q^{-}=q \tag{1}$$

Where the (+/-) superscripts refer to corresponding side of the heat front, based upon the created coordinate system. Equation (1) is then applied with the appropriate boundary conditions based on whether a constant heat flux or temperature is imposed at the leading edge. This equation is then dimensionalized in order to account for the moving coordinate system. By using the moving coordinate system, a quasi-steady solution can be found which was the main goal of the study [23]. Two broad classifications are looked at and then subsequently divided further into more specific problems: Class A – imposed temperature at the heat front and Class B – imposed flux at the heat front. A table in the study gives the exact solutions to six different cases within each class that were based upon different heat dissipation coefficients, the latent heat for melting or freezing, and the melting temperature of the material. Since this is a very simplified problem, it cannot be directly applied to welding to get accurate results, but it is a good starting point.

The next step in the evolution of the heat source modeling comes by way of the 2-D Rosenthal solution [20]. This solution looks at a moving point heat source in a quasi-steady state scenario. Since the heat source is modeled as just a moving point, the distribution of power within the radius of the heat source, which in our case as well as in [20] is a laser, is neglected. This acts as an infinite power density. It was found that this assumption is a reasonable one when the melt pool geometry is much larger than the laser

beam as would be the case in the building of thin wall structures in the LENS process. The Rosenthal solution then arrives at:

$$\overline{T} = e^{-\overline{x}_0} K_0 \sqrt{\overline{x}_0^{-2} + \overline{z}_0^{-2}} \tag{2}$$

with the normalized values of:

$$\overline{T} = \frac{T - T_0}{\alpha Q / \pi k b}, \ \overline{x_0} = \frac{x_0}{2k/\rho c V}, \ \overline{z_0} = \frac{z_0}{2k/\rho c V} \tag{3}$$

Where αQ is the absorbed laser power, V is the velocity, and K_0 is the modified Bessel function of the second kind, order zero, T is the temperature and x_0 and z_0 are the coordinates used in the problem. The remaining variables ρ, c, k, and b correspond to the density, specific heat, thermal conductivity and thickness of the material, respectively. This type of solution allows for easy creation of process maps that examine the solidification and cooling rates of the materials. One slight drawback to this type of solution is that temperature dependent material properties are not considered. Instead, linear or constant relationships are employed in order to simplify the problem.

Duley [10] sites the Rosenthal solution to the heat transfer equations, as seen in equation (4) as a jumping off point in order to find the conduction threshold for different materials. From this solution, a critical value for the velocity can be found based on the material properties of the work piece including melting temperature, conductivity, diffusivity and the absorptivity.

$$T(r) - T_0 = \frac{AP}{2\pi K r} exp\left[-\frac{v(x+r)}{2k}\right] \tag{4}$$

Where A is the absorptivity, K is the thermal conductivity, κ is the thermal diffusivity, v is the velocity of the heat source, r is the radial coordinate, and P is the power.

If we expand the Rosenthal solution by allowing the power to be represented by equation (5)

$$P = \int_0^\infty I(r) 2\pi r dr = 2\pi I(0) \int_0^\infty \left(exp\left[\frac{-2r^2}{w^2}\right]\right) \tag{5}$$

Where w is the radius of the beam focus on the surface, we can then take into account a distribution of the power as opposed to an infinite density as a single point. A more developed version of the two-dimensional heat source in this case, would be to use what is called a Gaussian distribution applied at the surface in order to model the power and heat dissipation of the laser [10, 17]. This type of source is used to model conduction

welding where the surface is never actually breached by the power of the heat source. This is quite different than its counterpart, which will be discussed next, keyhole welding. The Gaussian distribution is not modeled below the surface so the depth of the work piece is only taken into consideration for conduction through the entire thickness.

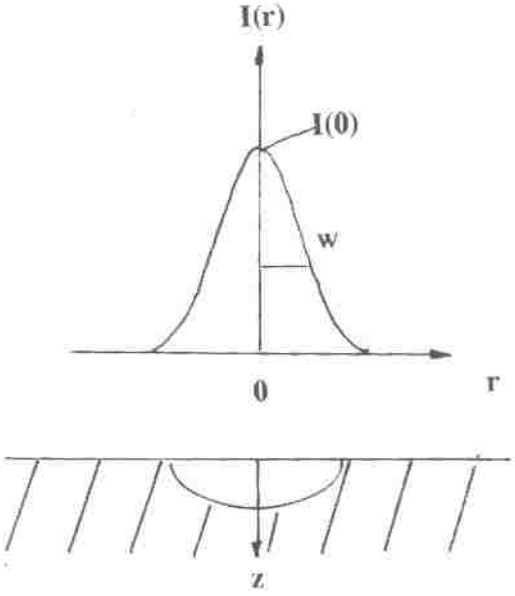

Figure 5 – Gaussian Distribution of Heat Source [10]

Figure 5 shows what this type of heat source would be modeled as where I(r) is the intensity of the laser beam. This of course makes sense in a logical standpoint that the laser would produce the most heat towards the center of the beam and less as one moves radially outward. Returning to the equations in order to find the critical velocity for conduction welding, equations (4) and (5) are then used to solve for the critical speed at which melting will occur:

$$v_m = -\frac{2\sqrt{2}\kappa}{w}\ln\left[\frac{(T_m - T_0)2\sqrt{2}\pi K w}{AP}\right] \quad (6)$$

This can be a very important finding as it gives a spring board from which to begin looking at the parameters needed for optimization. Once the heat transfer at the surface is found, it can be viewed as an induced heat flux, similar to the first source type discussed except it will now be translated downward into the material. This is where the melt pool shape arrives. The Gaussian distribution is one of the more prevalently used models when it comes to laser welding.

An even further developed type of heat source, which is also a highly acceptable model for welding heat inputs, is the 3-D double ellipsoid model [21]. This is a weighted type of distribution so that more of the heat flux is toward the front of the weld pool, i.e. the leading edge of the velocity, which gives a more circular ellipsoid, while the remaining heat source is distributed in a more elongated ellipsoid trailing in the rear quadrant. These two sections of heat flux distribution were given as [21]:

$$q_f(x,y,z) = \frac{6\sqrt{3}f_f Q}{abc_f\pi\sqrt{\pi}} e^{-3\frac{x^2}{a^2}} e^{-3\frac{y^2}{b^2}} e^{-3\frac{z^2}{c_f^2}} \tag{7}$$

$$q_f(x,y,z) = \frac{6\sqrt{3}f_r Q}{abc_r\pi\sqrt{\pi}} e^{-3\frac{x^2}{a^2}} e^{-3\frac{y^2}{b^2}} e^{-3\frac{z^2}{c_r^2}} \tag{8}$$

Where a, b, c_f and c_r correspond to the dimensions in the x, y and z directions as seen in Figure 5, f_f and f_r are the fractional factors by which heat is distributed among the front and rear quadrants with the requirement that $f_r + f_f = 2$, and Q is given as:

$$Q = IU\eta \tag{9}$$

With current I, voltage U, and efficiency η, giving the total power absorbed over the geometry.

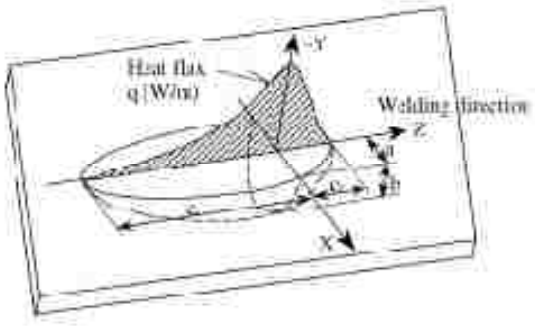

Figure 6 – Double Ellipsoid Heat Source [21]

The constants that define the size and shape of the heat source are vital to determining the geometries of the fusion zone (FZ), where the melting and welding actually take place, and the heat affected zone (HAZ), which was discussed earlier. Once these parameters are found to be satisfactory:

$$k\left(\frac{\partial^2 T}{\partial x^2} + \frac{\partial^2 T}{\partial y^2} + \frac{\partial^2 T}{\partial z^2}\right) + Q_{\text{int}} = \rho c_p \frac{\partial T}{\partial t} \tag{10}$$

Will give the non-linear heat transfer, where ρ is the density, c_p is the specific heat, and k is the conductivity of the material. Once the heat transfer into the weld pool area is

found through equation (10), the heat transfer to the surrounding areas (HAZ) can be found. This transfer is by way of both convective and radiant rates. It has been found that the double ellipsoid method is best for arc welding such as MIG (metal inert gas) and TIG (tungsten inert gas), but it is still relevant to see all the possibilities of modeling before deciding on a final selection.

The final scenario of heat source modeling, keyhole welding [10, 22], was mentioned earlier as the counterpart to the Gaussian distribution or other heat flux sources induced at the surface. Keyhole welding, which is also often used in the modeling of laser welding, occurs when there is penetration of the surface by the heat source. Duley [10] examines the threshold at which this takes place and gives a glimpse into what actually happens. Although Duley admits that it is not a subject that is greatly understood, it is known that the process begins with vaporization at the surface. Therefore the vaporization temperature can be found as:

$$T_v - T_0 = \frac{A_v I(0)}{K_v (2\pi)^{1/2}} \tan^{-1}\left[\frac{8K_v t}{w^2}\right] \tag{11}$$

Where explanations of the initial variables can be found following equations (4) and (5) discussed earlier and the subscripts applied to said variables represent the values around the vaporization temperature. It has been found that this threshold depends on the radius of the laser and the duration of any pulse that is occurring. This becomes independent of time in cases of long pulse length or constant durations of laser emittance [10]. The threshold can also be further facilitated by the surface tension and convective flow in the weld pool, which was also discussed elsewhere as the Marangoni effect [10, 42]. Through this phenomenon, material gathers around the perimeter of the weld pool, thereby acting as a lens focusing the laser power at a more concentrated power level, causing the vaporization to occur at a more rapid rate, which obviously results in a deeper penetration in the weld pool [10]. This motion can often become turbulent, as found by Wang et al. [22]. But the degree of turbulence is not very high as the eddies within the melt pool were not found to be very large. This theory and its effects will be discussed further in a following section. By finding the pressure difference at the front and trailing edge of the weld pool, a velocity profile can be found that explains the magnitude in certain locations of the pool. This profile shows a circulation effect caused by the pressure difference that was observed to provide a possibility of “closing” the keyhole.

Duley [10] also examines the motion within the moving keyhole and provides an explanation for instabilities that result within the melt pool. The following equation (12) shows the velocity normal to the surface and parallel to the motion of the heat source.

$$v_d = \left[\frac{\kappa}{w}\frac{\rho_t}{\rho_s}\left(\frac{2u_g}{L_v\rho_l}\right)\left[I_\alpha - \frac{Kv}{\kappa}(T_v - T_m) - \frac{\gamma}{w}\right]\right]^{\frac{1}{2}} \quad (12)$$

Where κ is the thermal diffusivity, u_g is the gas velocity due to the vaporization in what is referred to as the Knudsen layer [10], I_α is the absorbed laser intensity, w is the beam radius, ρ is the density, γ is the surface tension, K is the thermal conductivity, L_v is the latent heat of vaporization, v is the velocity of the heat source, and the subscripts s, l, V, t, m represent solidus, liquidus, vaporization, transition, and melting, respectively. Equation (12) can therefore best be used in order to predict the shape and location of the front wall of a melt pool.

Now that the widely accepted methods for heat source modeling have been discussed, methods of applications to full scale models can now be investigated. The first methodology that will be looked at will be the application of numerical analysis to the modeling of the welds. These studies [9, 18-19] usually involve some form of specialized computer code that runs the computations required for the heat and fluid interactions. The first study from Dye et al [9], which was already examined for its findings in the realm of weldability, employed numerical modeling into to obtain such results. Dye et al used some fairly complex equations of heat transfer in order to calculate the different criteria for the weldability analysis.

$$T(x,y,z) = T_0 + \frac{q}{2\pi\kappa\sqrt{x^2+y^2+z^2}} \times exp\left\{-\frac{v}{2\alpha}\left(x + \sqrt{x^2+y^2+z^2}\right)\right\} \quad (13)$$

Equation (13) shows the heat transfer model for a point source on a semi-infinite plate where x, y, and z are the coordinates employed, q is the effective power, T_0 is the nominal ambient temperature, κ is the thermal conductivity, and α is the thermal diffusivity [9]. This equation is then ramped up in order to take into account a Gaussian distribution type power source:

$$T(x,y,z) = T_0 + \frac{q\alpha}{\pi^{3/2}\kappa} \times \int_0^\infty \frac{exp\left\{-\frac{[(x+vt)^2+y^2]}{(s^2+4\alpha t)} - \left(z^2/4\alpha t\right)\right\}}{\sqrt{\alpha t}(s^2+4\alpha t)} dt \quad (14)$$

With s being the distance from the heat source when the power density falls to 1/e of

its maximum value. The complication arises with the solving of the integral; therefore the numerical modeling is employed. These results are then tabulated and compared to material data in regards to the phase diagram. This allowed Dye et al to predict the failure modes, which were discussed previously, that may arise in certain scenarios.

The next two studies by Ye et al [19] and Wang and Felicelli [18] both take a close look at the building of thin walls using the deposition feature of the LENS process. It is interesting to note the contrasts and comparisons of these two studies as they are looking at essentially an identical process, especially since both teams use a stainless steel as the experimental material. Wang and Felicelli [18] have a much more simplistic calculation that they employ. A two-dimensional model is used to represent the thin wall. Figure 7 shows how the heat source was applied along the top surface of the wall. With this model a finite element method is employed to solve the two-dimensional equation:

$$\frac{\partial T}{\partial t} = \kappa\left(\frac{\partial^2 T}{\partial x^2} + \frac{\partial^2 T}{\partial y^2}\right) - \frac{L}{C_p}\frac{\partial \varphi}{\partial t} \tag{15}$$

Where T is the temperature, t the time, κ the thermal diffusivity, L the latent heat of melting, C_p the specific heat and φ is the volume fraction of liquid given as:

$$\varphi \approx \frac{T - T_S}{T_L - T_S} \tag{16}$$

Where the subscripts S and L correspond to the solidus and liquidus temperatures.

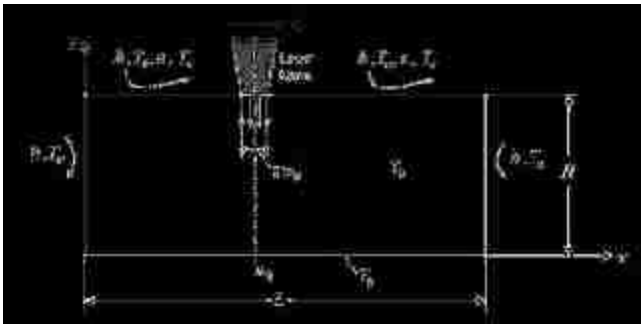

Figure 7 – Schematic of Two-Dimensional Model [18]

Figure 7 shows the two-dimensional model that Wang et al used. Several assumptions were put in place in order to validate the use of such a model. First, that there would be no heat loss through the front or back of the piece. This can be considered a fair assumption since a majority of the heat transfer takes place down into the piece or at the trailing edge of the moving heat source. Next, the heat loss due to radiation was not taken into account. This is an important factor to keep in mind as the study found that heat

dissipated by means of convective and radiant transfers tabulated to around 9% of the total heat dissipated [18].

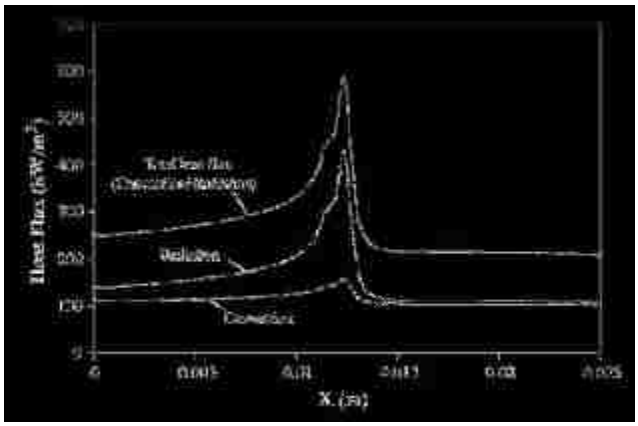

Figure 8 – Heat Flux Distribution along Top Surface [18]

As seen in Figure 8, by not taking radiation into account, the calculations are greatly simplified and may lose some accuracy in the results portion. An interesting note that followed disregarding the radiant heat transfer mode was the several different thermal conductivity values were considered. This is not nearly as effective as using a non-linear mapping of the thermal conductivity value as a function of temperature, but it was at least still taken into account during some aspect of the calculations. Another limitation that was put in place was that there could not be a direct correlation between the power that would be absorbed through a three-dimensional model and that with the much simplified two-dimensional version. This study could be looked at as a base line for computation where the complexities will increase as the discussion furthers. As we turn our attention to the results from Ye et al [19], we will notice an evolution of the calculations as they examine a three-dimensional model. This study used integral equations in order to solve a transient problem over specified time steps. An initial condition was specified and the equations of integration were solved. Those results were then employed as the new initial conditions for the following time step.

Employing Fourier's Law of heat conduction and applying it to the heat equilibrium equation:

$$\int_V \delta T\, \rho \dot{U}\, \mathrm{dV} + \int_V \frac{\partial \delta T}{\partial \vec{x}} \vec{k} \frac{\partial T}{\partial \vec{x}}\, \mathrm{dV} = \int_S \delta T\, q\, \mathrm{dS} + \int_V \delta T\, r\, \mathrm{dV} \qquad (17)$$

Where δT represents an arbitrary variational temperature field, T is the temperature at a given time step, U is the internal energy, q is the heat flux vector per unit of area, r is

the heat flux per unit volume generated by the body, and ρ is the mass density of the material [19]. In order to properly create the mesh and nodal points, a commercial Finite Element Method (FEM) software package, ABAQUS, was used. An algorithm within the program allowed for the computation in the specified time step manner. Since this study is very similar to the previously discussed one in that the main goal is to model the building of a thin wall using the LENS process, some of the simplifying assumptions are repeated. First, the material property values were not considered to be temperature dependent thereby eliminating the non-linear aspect of the calculation. Next, only heat conduction in the wall and the base substrate would be considered. Therefore, once again, the effects of radiant heat transfer are ignored, while the last important assumption of the part being adiabatic eliminates the concern for heat transfer out through the sides of the thin walled structure.

From here, we can concentrate more on the abilities that certain commercially available codes have and how some studies employed those resources. One of the more prevalent codes in the area of welding models is SYSWELD [13-17]. This software package has CAD and meshing tools built in as well as a database of material properties for easy application. It also boasts an easy Graphical User Interface (GUI) with "wizards" that direct the creation of the problem. It can then perform the heat flow calculations as well as the mechanical effects caused by the temperature loads.

L. Wang and S. Felicelli are both involved in three of these studies where the model was based once again on the thin plate deposition [13-15]. These three studies used a 10-pass method of deposition in order to build the thin walls using stainless steels in the LENS process. A Gaussian distribution was used in order to represent the heat input for the model. The teams all employed an interesting technique in which the ten layers were created in the CAD/mesh file, but the material properties were edited in order to mimic the deposition and appearance of a new layer. To do this, the materials were assigned "dummy" values in which the thermal conductivity was extremely low and therefore the materials could not heat up as the heat source passed across them. As the materials were supposed to appear, they were "activated" and given the proper material property values that could obtained from other literature sources. This technique allowed the teams to visualize the effects of continuous heating of a material as the heat sources were designed

to melt one and a half layers per each pass so that the layers could melt and join together properly. Wang et al [14] actually investigated this problem a little more in depth by adding in the material science aspect of the different phases of a material and using the appropriate material properties in order to get an even more accurate model for the residual stresses and deformations that occur as a result of the weld passes.

The study by Park et al [16] describes a different scenario for the application of SYSWELD. In this study, a Rene single crystal nickel-based alloy is used to model the repair of a crack. This was accomplished by created a model with a single groove that extended the length of the model. This groove used a similar technique to the previous SYSWELD studies by using an "activation" process. In order to accomplish this task the team assigned the material in the groove as having zero-mass initially but as the heat source passed the then active element would revert to the material properties that it should possess. Also similar to [14], Park et al examine the appearance of different phases in the weld pool as well as HAZ. This allows for better prediction of the deformation and stress/strains. This is much closer to the case that will be presented in this paper as cracks are a major issue that needs to be addressed in the repair process.

A final way in which the welding process can be modeled is through a finite difference method. This was employed by DebRoy et al [26] and their team in order to gather calculated data for temperature distribution. The team could then use this data in order to plot the thermal gradient which influences grain growth. In this study, a FORTRAN computer code was created in order to compute the temperatures and fluid velocities at each node through an iterative approach. These calculations were based on the conservation of momentum and continuity equations. Once the values were found, a series of "correction" factor equations were used for the pressure and velocity values. This took into account the dimensionalization of the problem and adjusted the values the answers so they can be used for the beginning guess of the next iteration. All this was performed using a modified SIMPLE (Semi-Implicit Method for Pressure-Linked Equations) algorithm which ends when the solution converges. Work with this program was also done by fellow Lehigh student Timothy Anderson [44] and will be a basis for comparison later in this work.

Turbulence

Regardless of the modeling technique used, there will inherently be issues in the selection of boundary/initial conditions as well as other factors. One of the major issues regarding the modeling of the weld pool is the determination of whether the fluid flow becomes turbulent or not. Turbulent behavior is a very difficult theory to understand, let alone to model. Several studies [22, 35-38] have shared their take on whether the model should be turbulent or not. One insight that appeared in all of these studies, and is shown in the lack of other available material, is that there is not a distinct cutoff criterion for turbulence when dealing with molten metal. Flows in fluids such as water are easily distinguishable as turbulent or not as there are well established criteria for Reynolds numbers which serve as transition points. As a result of the lack of well documented criteria for determining if a molten flow is turbulent or not, the decision often rests with the researchers that are creating the simulations to assume one way or another. If the weld pool is found to be turbulent according to an assumed flow criterion, then many effects can be seen. One such criterion that has been developed was a new turbulent Reynolds number [38] as seen below in Equation 18.

$$Re_t = \frac{\sqrt{kl_0}}{\nu} \tag{18}$$

Where k is the turbulent kinetic energy, ν is the kinematic viscosity, and l_0 is the turbulent length given by:

$$l_0 = k^{3/2}\varepsilon \tag{19}$$

Where ε is the turbulent dissipation rate. This can be used as an influence for the assumption, but as stated previously and again in this study, there are no definitive criteria for determining if the flow is turbulent or not. In [36] Atthey examines the modeling of an arc process. In this study another way to determine if a system is turbulent or not is to perform a stability analysis as this would not be influenced by any sort of assumptions. This unfortunately is not an easy task and therefore not a very viable solution. As an additional piece of information for the argument that there is no definitive value for determining turbulence, Atthey cites another work which states that the Reynolds number could be reduced or increase due to the effects of "numerical diffusion."

Once an assumption is made and a system is determined to be turbulent, some

expected outcomes must be known. First, and most importantly, the presence of turbulence in a model can greatly affect the depth that is calculated. Laminar flow models have been found to highly overestimate the pool depth when compared to the experimental results [11, 37]. Therefore turbulent flows show more shallow pool depths as the effective viscosity of the molten metal increases ($\mu_{eff} > \mu_0$) and the convection slows down. Another material change occurs as the effective thermal conductivity increases ($k_{eff} > k_0$) and effect of convection thereby decreases [11]. This result was also examined by Choo and Szekely [37] but no definitive guidelines for exactly how much the effective material properties increase. The effective amounts were found to be:

$$\mu_{eff} = \mu + \mu_t \tag{20}$$

$$k_{eff} = k + k_t \tag{21}$$

Where the subscript *t* corresponds to the turbulent addition term and the values without subscripts are the values corresponding to the known metallurgical material properties. Large ranges for additive terms0 were given for the effective viscosity while a relation between the two is given by:

$$Pr_t = \frac{C_p \mu_t}{k_t} = 0.9 \tag{22}$$

Where Cp is the specific heat of the material. Choo and Szekely state that the amount of increase is based on the amount of turbulence. For example, the model used for the study was determined to be mildly turbulent so an increase of around 30 times the molecular viscosity was used. In so called highly turbulent systems, as would be the case in an induction furnace, increases on the order of 100 or 1000 times the molecular value could be found. Another finding of the study states that the velocity at the free surface as well as the free surface temperature will both be reduced when turbulent conditions are employed in the modeling. Charkraborty et al [35] also examine the effects of using a turbulent flow model. One observation that was noted in this study was the effect of the directional torch movement was greatly diminished. This is due to the enhanced thermal diffusion which is non-directional in nature. Not only was the maximum temperature reduced, as cited by [37], but the temperature distribution isotherms were also greatly affected in that they looked very similar those that would be found in a model that used pure conduction. This change in isotherm pattern leads to a difference in the temperature gradient which can have a profound effect on many other properties within the weld pool

such as cooling rate and Marangoni convection. This is a very important finding as it will be discussed later that the surface tension is one of the main driving forces in our problem, giving a Marangoni number as one of the dominant non-dimensional numbers.

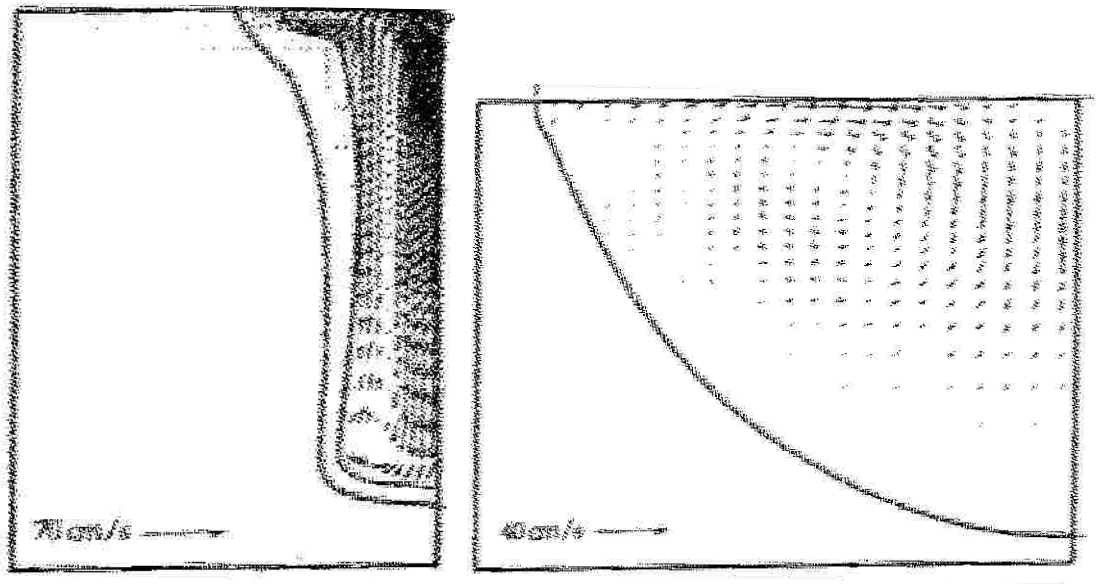

Figure 9 – Reprint from [37] Comparison of Turbulence Effects

Figure 9 above shows the comparison between the weld pool shapes that will be predicted using laminar (left) and turbulent (right) based assumptions. These figures show the velocity profiles but the overall shapes are applicable to the isotherm patterns as well.

Many studies that involve arc welding simulations [35-37] will assume that the model should be turbulent based upon the disturbances that are created by the high current values. Lorenz forces, caused by current that creates a magnetic field, are often the culprit. This value can be found through Maxwell's equations which gives the Lorenz force as the cross product (**J** × **B**), where **J** is the current density and **B** is the magnetic flux density. With all the current that flows through the work piece during an arc process, this value can become rather high. This value is then added into the conservation of momentum equation as a body force distribution [35]. In Choo's and Szekely's study [37], they look at a couple influences that could cause the turbulent behavior in arc welding processes. The first is the pressure gradient that occurs within the arc due to the plasma interactions. Another contributing factor to the turbulent regime transition could also come by way of the shear forces at the surface causing instabilities. This happens

due to the high free surface velocities that occur within the pool as well as the flow of the gas in the arc that causes a shearing effect. In the study by Wang et al [22], the assumption was made that the keyhole modeling technique caused instabilities in the system that would result in turbulent flow. As cited by Kou [11] the keyhole essentially acts as a black body and traps the energy. This occurs as the beam (electron or laser) is reflected off of the newly exposed surfaces, instead of just hitting the top surface directly and heating downward. To return to the study by Wang et al [22], one the assumptions that was made stated that the flow was turbulent and incompressible. In addition to this statement, the weld pool surface was assumed to be flat. This last portion does not completely make sense as stated earlier; the keyhole process often begins with material flowing to the edges due to Marangoni effect caused by the surface tension. By this information, the assumption made by Wang et al seems to be one for great simplification purposes.

Once it is decided that the flow should be assumed turbulent, the next step is choosing one of the many modeling types that should be employed. The first, and most prevalent, method is the use of the k-ε equations [22, 35, 37-38]. As mentioned earlier, k is the turbulent kinetic energy and ε is the turbulent energy dissipation rate. This is the main example of a two-equation method, where the number refers to the quantity of partial differentials, for solving a turbulent flow problem. It is also one of the more accurate and universal methods. According to the theoretical portion of the Fluent, Inc. tutorial [43] there are also many variations on this standard k-ε model. These variations are often catered for specific models and involve deeply rooted assumptions that make them inapplicable to general cases. For further knowledge of these models it is encouraged that one refer to the literature as these models will not be used in the current work. Zero-equation models are also used from time to time. As the name states, there are zero partial differentials in these models which results in the use of algebraic equations only to create relationships between μ_t and the flow values.

Secondary Flows

Another aspect to consider in the discussion of fluid modeling is the presence of secondary flows. Since the actual motion within the weld pool is hard to capture in a visual sense, other studies that can be related to the molten metal in the weld pool must be examined. One such study was performed by Muite [45]. In this study, secondary flows were examined with small Reynolds numbers in rotating circular lids with small aspect ratios. When the Reynolds number was below 500, the flow was dominantly azimuthal with secondary flows traveling towards the outer radius, down the fixed wall, along the bottom of the lid, and finally upward in the axial direction to return towards the surface. A similar flow type has been found in several studies [11, 35-37] where the fluid flow in the weld pool was modeled. This was often found to be driven by the surface tension through the Marangoni effect. With Reynolds numbers above 500 but below 1000, the secondary flow pattern slightly changed in the circular lid by flowing downward in the axial direction first where a stagnation point was created. After this, a bubble was found to form and have circulation opposite that of the lid [45]. An interesting discovery was found in this study in that discontinuities in the Reynolds number did not have a profound effect on the flow patterns. This is interesting to note as the velocity and material property values within weld pools can have fairly large variations across a small area. Muite also draws a comparison to flows that were studied in rectangular cells, similar to [38], and concludes that as the aspect ratio increases, so follows the number of eddies that can be seen. The main difference is the centrifugal forces that dominate the field as the driving force. These are interesting discoveries to keep notes of and try to relate to the weld pool geometry.

Material Choices

One of the more important parameters in the discussion of welding is the material choice for a filler metal, if one is needed at all. Some processes, such as SMAW and GMAW, use a consumable electrode as mentioned earlier. By using these types of methods the filler metal is heated due to the arc and resistive heating and therefore can be introduced directly into the weld pool near the same temperature. This helps to increase the melting efficiency since energy is not lost from the weld pool when filler metals that are not near the proper temperature are introduced [11]. This efficiency can be found by:

$$\eta_m = \frac{E_{fz}}{E_w} \tag{23}$$

Where E_{fz} is the energy that is in the fusion zone and E_w is the energy that makes it to the weld surface from the heat source. Once filler metal in the non-consumable electrode technique enters into the equation, E_{fz} is reduced; thereby decreasing the overall efficiency of the process. This gives way to a limit on the efficiency arc welding techniques can attain. Another aspect to consider in the consumable electrode processes is the mode in which the molten metal transfers to the weld pool. At lower currents the transfer mode is in droplet form or globular transfer while at higher currents the metal may start to heat up beyond a certain threshold and explode resulting in spray transfer mode [11, 40]. This introduces an interesting concept into the modeling portion of welding in that momentum and mass flux could contribute to the overall heat transfer and fluid flow.

Moving on to high energy density techniques, we will only discuss laser welding as the electron beam process cannot use a filler metal, otherwise it will interfere with the flow of electrons. Within the LENS process there are three main options to choose from. First, the obvious choice of an autonomous weld performed without the addition of any mass. This could be used in order to fix small imperfection cracks by using a keyhole process past the depth of the crack. Second, filler metal could be introduced into the system in the form of powder. This form of deposition is the most common form in the LENS process. Two different studies take an in depth look at the powders that could be used for the LENS process [24-25]. The first by Schwendner et al [24] looks at the implications of using a blend of powders in order to achieve specific material properties. In this case, the study was aimed at creating an alloyed metal part by employing

elemental powders and depositing an alloy in situ instead of depositing pre-alloyed powders. An experiment was performed in order to compare the outcome of two different binary alloys: Titanium-Chromium and Titanium-Niobium. The main difference that was examined was the enthalpy of mixing that each of these systems possessed. Ti-Cr had a negative enthalpy of mixing while Ti-Nb had a positive value. This proved to be a major difference in the homogeneity as well as the solidification structures of the final part. A contributing factor to the homogeneity was that the powders were left in the same hopper. With separate hoppers, the mass flow rate of each of the powder systems could be controlled independently thereby reducing the effects of percolation of alloying elements within the elemental powders. The final discovery was that the systems with a negative enthalpy of mixing will have rapid solidification rates which severely affect the microstructure of the part. This is due to the fact that the powder system actually absorbs energy away from the melt pool.

A study by Susan et al [25] examined the porosity effects that powder deposition has on LENS part builds. The team noticed different types of porosity in different structures. The first type was lack-of-fusion (LOF) which occurred at the boundary between layers of a build. This defect is characterized by an elongated shape between passes of the LENS. The other type was intralayer porosity where voids formed within one pass of the laser. This defect often appears in a spherical shape which would suggest a gas bubble created the void. In order to attempt to find a correlation between these defects the team took a closer look at the metal powder. The first explanation explored was that powders that are used in the LENS process are often gas-atomized. This production process uses an atomizing gas, such as Argon, that can create voids in the particles in which the gas could become trapped. Gas could also enter the weld pool through contamination by the powder feeder itself. These feeders employ pressurized gas in order to force the powder in the system. In order to find the relation between the starting powder porosity and the porosity of the final product, experiments were conducted using different lots of stainless powders and creating different patterned structures with a thin wall and a block with alternating direction layers. By keeping the process parameters consistent and creating parts with different heat flow patterns the effects of the porosity of the powders can be isolated. Travel speed was not found to have a profound impact on the porosity of the

part while the structure that was created affected which defects were more prevalent. With the thin wall pattern LOF did not appear while LOF was very common near the substrate surface in the block build. It was discovered that the pores in the final product were larger than those in the initial powder but the quantity was less. This led to the belief that the gas trapped in the powder voids could accumulate in the melt pool, creating the larger pores. Although it was found, after comparing the data for the all the experiments, that there was a direct tie between the porosity of the powder and that of the final part, no definitive quantitative relation could be developed. In general the larger the size of the pores in the powder the less porosity that appeared in the part. This could be attributed to a buoyancy force that has been found to increase with pore size. But again since this is not an exact correlation, the best solution that was proposed was that the surface of the part could be re-melted again with the laser in order to remove some the voids. This was performed by the team and the results were indeed favorable.

In addition to powder deposition a wire similar to those employed in non-consumable electrode techniques can be used for the addition of mass as a filler metal. According to Duley [10] the filler wire system is fed in at an angle of around 45° and intersects the laser near the focal point. As expected, and mentioned in the earlier discussion about the introduction of filler metal wire into the weld, the wire can significantly affect the efficiency and depth at which the laser can operate. An interesting role for the filler metal is to also replace certain properties that may be lost during the process. Duley [10] cites an example of Aluminum alloys that need Mg and Si to be reintroduced into the system in order to gain weld strength as well as minimize the porosity.

Grain Orientation Effects

Once the heat transfer has been properly modeled the cooling rate can be found. This section discusses the metallurgical aspect of welding by examining the Heat Affected Zone (HAZ) more in depth as well as how the cooling rate governs the microstructure formation and growth in the weld metal. This section is very important when discussing the impact of welding on a material's strength and durability. Kou's book [11] explains the metallurgical aspect of welding very thoroughly from a material science aspect. It examines the composition of liquid and solid in the partially mixed zone as well as how the fluid in the weld pool begins to solidify. From material phase diagram information, the temperature gradient found in the weld pool, and the growth rate of the grains one can calculate the criteria for constitutional supercooling. This phenomenon occurs when the actual liquid temperature is below the liquidus line. There are other theories on how the creation of different microstructure patterns forms but they are neither popular nor easily supported, therefore they will not be discussed in this work. From the phase diagram point of view, this undercooling takes place in the region where solid and liquid coexist or what some refer to as the "mushy zone." The four main types of solid-liquid (S/L) interface morphology that arise due to undercooling are: planar, cellular, columnar dendritic, and equiaxed dendritic. Planar growth is the preferred type in the realm of single crystal repair since the grains will grow in the same direction as the base metal which will allow the material to retain its original properties. Deviations start to occur as the temperature stays below the liquidus line and the growths that form are no longer melted back by the higher temperatures. This allows cellular arms to form. As undercooling increases, smaller arms branch off of these cellular arms to form the columnar dendritic mode. This continues until the limit, often referred to as the Columnar to Equiaxed Transition (CET), given by:

$$\frac{G}{R} \geq \frac{\Delta T}{D_L} \tag{24}$$

Is reached and nucleation occurs as equiaxed dendrites form. Where in Eq. (24) G is the temperature gradient, R is the growth rate of the grains, ΔT is the temperature difference at the equilibrium freezing range given by $\Delta T=T_L-T_S$, and D_L is the dilution coefficient of the liquid. This results in a dramatic decrease in strength as well as an increase in the opportunity for cracks to form. In order to avoid this issue the cooling rate needs to be

adjusted so that the time that the material experiences undercooling is shortened. Cooling rates are influenced by the heat input values of the process given as:

$$HI = \frac{\eta_a P}{S} \tag{25}$$

Where P is the power input, S is the travel speed of the heat source, and η_a is the anode efficiency given as:

$$\eta_a = \frac{E_W}{E_{HS}} \tag{26}$$

Where the subscripts W and HS correspond to the weld energy and the energy from the heat source, respectively. Another effect that the heat input value has on the grain structure comes as a result of the fact that grains want to grow perpendicular to the S/L interface. As the heat input decreases with higher travel speed, the weld pool becomes shaped more like a teardrop. This creates a boundary along the centerline of the solidified weld area which again decreases the strength. With lower travel speeds, the weld pool becomes more elliptical and the grains will grow in a curved fashion in order to catch up with the S/L interface. Another effect that the travel speed has is on the cooling rate through the equation:

$$\varepsilon = G \cdot S \tag{27}$$

Where ε is the cooling rate and G and S have already been defined previously. The cooling rate directly affects the dendrite arm spacing by:

$$\lambda = A\varepsilon^{-n} \tag{28}$$

Where A and n are given constants based on the material. Equations 24-28 therefore reinforce the importance of being able to model the welding parameters accurately. Several studies have examined this in more specific cases as applied to superalloys. The first by Vitek et al [27] looks at Nickel-based superalloys and quite directly answers how to avoid stray grains and why. Stray grains can be defined as those that do not align with desired the crystallographic pattern. As the single crystal structure of the superalloys is vital to the performance of the material and the introduction of grain boundaries decreases the resistance to many loads that the material may encounter, CET must be avoided. The first interesting note in this study is that a simple Rosenthal solution was employed in order to calculate how the grains will form. The simplicity and symmetry of the model were the reasons this choice was made. By then employing the

aforementioned criterion for constitutional supercooling the area fraction of growth by stray grains could be calculated by:

$$\Phi = 1 - e^{S} \quad \text{with } S = \frac{-4\pi N_0}{3}\left(\frac{1}{(n+1)(G^n/aV)^{1/n}}\right)^3 \qquad (29a, b)$$

Where the only new variable to be defined is N_0 which is nucleation density while A and n continue to represent constants. The team arrives at a value of $\Phi<0.5$ in order to have epitaxial growth while avoiding equiaxed microstructures. The study found that the likelihood of stray grain formation is highest at the centerline of the weld while the lowest value was found to occur at the fusion line of the pool. This is a result of the thermal gradient being highest at the fusion line. Experiments then verified the calculated predictions and showed that lower power inputs and higher travel speeds, which would translate to a low overall heat input, would be the optimum parameters to avoid stray grain formation. Another discovery was that the orientation of the weld as compared to the orientation of the grain direction in the base metal had negligible effects on the formation of stray grains. Gumann et al [28] performed a similar study in which the prediction of stray grains was calculated using the same criteria as Vitek et al [27]. Gumann et al [28] then compared the predictions to results from a process called epitaxial laser metal forming (E-LMF). This process is essentially the same as any other LMF process but there is increased concern with the parameters that are selected to ensure the proper growth. Special concern is also involved in the re-melting of the layer below the one being deposited. This helps to ensure consistency of the proper growth or epitaxy between layers. One way the team hoped to increase their ability to achieve this scenario was to preheat the base metal; which in this case was the Ni-based superalloy CMSX-4. This was also done in an attempt to avoid solidification cracking. Unfortunately the calculations and experiments pointed against this idea and said that preheating should be avoided while the beam power and radius should be minimized. These factors all help to keep the temperature gradient low.

Two other studies [29, 30] examine the grain structure morphology in a more general sense by discussing the effects that morphology has on the physical properties of the material. The first study, performed by Saas et al [29], tested how the grain orientation direction of CMSX-4 impacts the physical properties of the material; most specifically the creep resistance. The high strength in Ni-based superalloys comes as a result of

precipitation hardening in the γ-phase matrix with γ' precipitates and the formation of these precipitates actually allows for these materials to gain strength at elevated temperatures. Knowing that these precipitates are present, the team focused on the effects of how they were orientated compared to the loading direction. The team discovered that the material demonstrated a high degree of anisotropy within the file, or in other words, that the orientation does indeed have a large impact on the performance. This impact decreases as the material leaves the primary creep phase, where the strain increases due to work hardening, and enters the secondary phase where the strain remains essentially constant and in which the overall life span of the material is controlled. This decrease in orientation effects occurs since the creep begins to affect the γ matrix more than the precipitates. Kondo et al [30] also performed a similar study with their examination of the effect of morphology on the creep resistance of CMSX-4. This studied differed from [29] as Kondo et al did not enter into the secondary phase of creep. Instead the team looked at the effect of prior-creep and the time that the material underwent the creep loading which lead to the investigation of how the material would be damaged due to the loading and how this would change the evolution of the morphology of the γ-γ' phases. It was then concluded that the creep resistance was not based necessarily on the orientation of the γ matrix but rather the dimensions of the channels between γ' precipitates as this had a direct correlation to the radius of dislocation curvature. It can be seen that the microstructures that form as a result of the thermal loading, that is induced during the welding process, has a dramatic effect on the performance of the material and therefore special attention must be paid to the process parameters that govern these scenarios.

Problem Statement

Now that the background for welding and all the effects that can occur as well as the modeling options have all been thoroughly discussed, the study can move onward to the actual problem statement. Since there is great interest in the area of welding simulations, it is most desirable to create a robust model that can accept the best known material properties and compute the fluid flow as well as the temperature distribution within the molten pool and the HAZ. Some models [26, 37, 44] use adjusted material properties based upon assumptions while this study aims to examine other aspects that could be changed and applied to a wide range of problems. In order to do accomplish this task, a finite element code will be employed to solve the coupled equations of heat transfer and fluid flow. These equations will be solved in a quasi-steady state scenario as many models are. This helps in the visualization as well as to eliminate terms that could vary with time. To begin, the basic governing equations that can be used for modeling steady-state heat and fluid flow [21-22, 26, 43] are given for each coordinate direction as:

Continuity Equation:

$$\frac{\partial u}{\partial x}+\frac{\partial v}{\partial y}+\frac{\partial w}{\partial z}=0 \tag{30}$$

Conservation of Momentum Equation:

$$\rho\left(u\frac{\partial u}{\partial x}+v\frac{\partial u}{\partial y}+w\frac{\partial u}{\partial z}\right)=\mu\left(\frac{\partial^2 u}{\partial x^2}+\frac{\partial^2 u}{\partial y^2}+\frac{\partial^2 u}{\partial z^2}\right)-\frac{\partial p}{\partial x} \tag{31a}$$

$$\rho\left(u\frac{\partial v}{\partial x}+v\frac{\partial v}{\partial y}+w\frac{\partial v}{\partial z}\right)=\mu\left(\frac{\partial^2 v}{\partial x^2}+\frac{\partial^2 v}{\partial y^2}+\frac{\partial^2 v}{\partial z^2}\right)-\frac{\partial p}{\partial y} \tag{31b}$$

$$\rho\left(u\frac{\partial w}{\partial x}+v\frac{\partial w}{\partial y}+w\frac{\partial w}{\partial z}\right)=\mu\left(\frac{\partial^2 w}{\partial x^2}+\frac{\partial^2 w}{\partial y^2}+\frac{\partial^2 w}{\partial z^2}\right)-\frac{\partial p}{\partial z}+F_b \tag{31c}$$

Conservation of Energy Equation:

$$\rho h\left(\frac{\partial u}{\partial x}+\frac{\partial v}{\partial y}+\frac{\partial w}{\partial z}\right)=k\left(\frac{\partial^2 T}{\partial x^2}+\frac{\partial^2 T}{\partial y^2}+\frac{\partial^2 T}{\partial z^2}\right)+S_h \tag{32}$$

Where *u, v, w* correspond to the velocity components in the *x, y, z* and directions,

respectively, ρ is the material density, p is the pressure, h is the sensible enthalpy, k is the thermal conductivity, S_h is the source energy term to account for additional heat from metal droplets, and F_b is the buoyancy force given as:

$$F_b = \rho g \beta (T - T_0) \tag{33}$$

Where g is gravity, β is the thermal coefficient of expansion, and T_0 is the reference temperature. This term came about due to the Boussinesq approximation which is used in problems where natural convection is present. This is an appropriate assumption as the temperature difference, and thereby the density difference, will be large due to the very high temperatures at the surface and ambient temperature further into the base metal. The buoyancy force was only considered in the vertical z-direction which is into the depth of the pool. The heat source travels in the x-direction and the y-direction is perpendicular along the surface of the weld. In equations (31a-c) the full original equations contained a source term that was reduced due to the specified quasi-steady state solution [26].

$$S_j = -\frac{\partial y}{\partial x} - \rho U_w \frac{\partial y}{\partial x} - C\left[\frac{(1-f_l)^2}{f_l^3+B}\right] u_j + F_j^e + F_j^b \tag{34}$$

It was further reduced by the fact that there will be no electromagnetic, or Lorentz forces, F_j^e, created by the laser in the LENS process that will be modeled. The terms that involved the motion of the work piece, U_w were also neglected. The remaining term with constants C and B represented dissipation of fraction-liquid in the mushy zone. This term was not taken into account for simplicity purposes in the finite element code that was used.

After the governing equations are known, the next step is to establish the appropriate boundary conditions. Many studies [10-11, 22] that looked at keyhole welding observed that the surface tension was a large driving force which corresponds to the Marangoni effect as mentioned earlier. This leads to the first boundary condition at the top surface:

$$\mu \frac{\partial u}{\partial z} = -\frac{\partial \gamma}{\partial T}\frac{\partial T}{\partial x} \tag{35a}$$

$$\mu \frac{\partial v}{\partial z} = -\frac{\partial \gamma}{\partial T}\frac{\partial T}{\partial y} \tag{35b}$$

$$w = 0 \tag{35c}$$

Where $\frac{\partial \gamma}{\partial T}$ is the surface tension gradient. This gives the free-surface boundary condition and the velocity constraints at the surface. Also at the surface, the heat flux boundary

condition needs to be established through Fourier's Law and the use of a Gaussian distribution yielding:

$$q = k\frac{\partial T}{\partial z} = \frac{fP\eta}{\pi r_b^2} e^{\frac{f(x^2+y^2)}{r_b^2}} \tag{36}$$

Where f is the power distribution factor, P is the laser power, η is the efficiency and r_b is the laser beam diameter. In addition to this heat flux condition the radiation of the surface must also be taken into account. This value is given by:

$$q = k\frac{\partial T}{\partial z} = \sigma\varepsilon(T^4 + T_0^4) \tag{37}$$

Where ε is the emissivity value, σ is the Stefan-Boltzmann constant, and T_0 is the ambient temperature. The final component of heat flux boundary condition is the limitations that take the symmetry of the system into account. The physical domain for the model is setup as symmetrical along the weld line. This forces the heat flux in the y-direction to be set to zero.

$$k\frac{\partial T}{\partial y} = 0 \tag{38}$$

The only other conditions that may be present would be initial conditions. This is not the case in the current problem, as time is not taken into account (i.e. steady state). Figure 10 below shows the basic domain of the problem, not drawn to exact scale, and shows where all the previous equations and boundary conditions are applied.

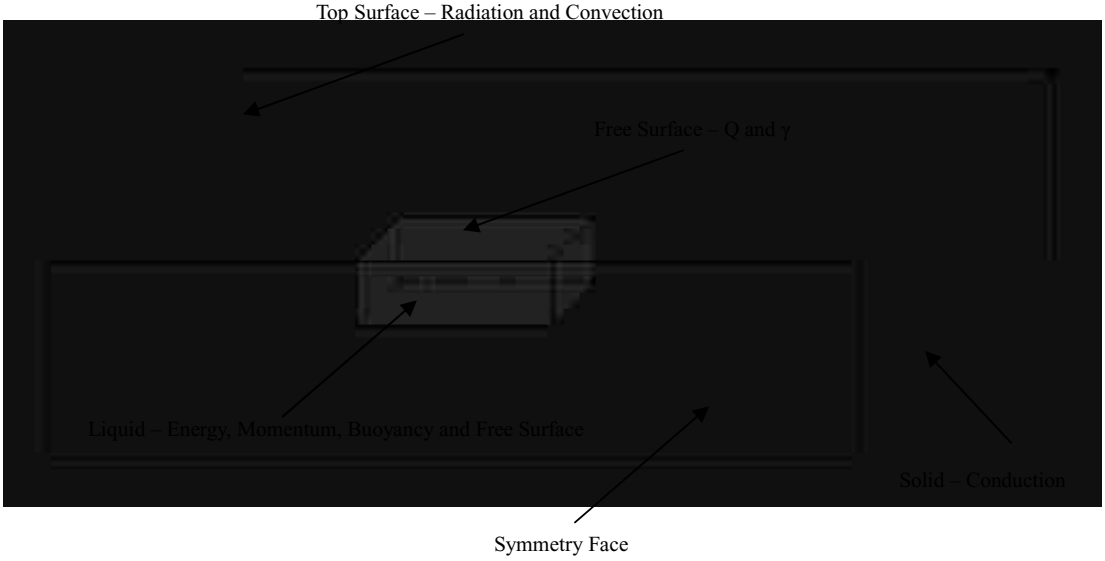

Figure 10 – Domains used for Model

The best way to compare the effects of certain parameters on the heat and fluid is through the use of dimensionless numbers. By comparing the magnitudes of these numbers the focus on certain welding parameters can be changed. In addition to this, the finite element code that will be used for this model, the commercially available FIDAP, requires that all parameters must be inputted as dimensionless values. The discretesization of the equations and boundary allows for easier convergence in non-linear problems such as in the weld pool by eliminating larger differences in magnitudes between the equations. By scaling the values, the tolerances that are created in the solution procedure can be arrived at in the appropriate number of iterations. As this is a common practice in the solution of fluid problems the usual pattern can be followed in the current study by starting off with scaling the position and velocity vectors with respect to an appropriate characteristic value. Using the Einstein notation the normalized velocities and lengths are found to be:

$$u_i^* = \frac{u_i}{U} \tag{39}$$

$$x_i^* = \frac{x_i}{L} \tag{40}$$

Where L is the characteristic length which was a chosen value based on comparison to the beam diameter and U is the characteristic velocity calculated by:

$$U = \frac{\alpha}{L} \tag{41}$$

Where α is the thermal diffusivity of the material. Taking these values and substituting into Equations (31a-c) and converting to Einstein notation gives [44]:

$$\mathrm{Re}\left(u^* \frac{\partial u_i^*}{\partial x^*} + v^* \frac{\partial u_i^*}{\partial y^*} + w^* \frac{\partial u_i^*}{\partial z^*}\right) = \left(\frac{\partial^2 u_i^*}{\partial x^{*2}} + \frac{\partial^2 u_i^*}{\partial y^{*2}} + \frac{\partial^2 u_i^*}{\partial z^{*2}}\right) - \frac{\partial p^{**}}{\partial x_i^*} + \mathrm{Re} Fr^{-1} g_i^* \tag{42}$$

Where Re is the Reynolds number defined as:

$$\mathrm{Re} = \frac{\rho U L}{\mu} \tag{43}$$

This corresponds to the dimensionless ratio between inertial and viscous forces. This is a very important dimensionless number since, as mentioned earlier; it sets the criterion for the transition from laminar to turbulent flow. Also in Equation (42) is the Froude number, defined as:

$$Fr = \frac{U^2}{gL} \tag{44}$$

And is the dimensionless ratio that captures the importance of inertial versus gravitational

forces. Finally, p^{**} corresponds to:

$$p^{**} = \frac{pL}{\mu U} \tag{45}$$

While g^* just becomes the unit vector in the direction of gravity which in the current case is the z^* direction. This process can continue and then be applied to Equation (32) to give:

$$\mathrm{RePr}\left(u^* \frac{\partial T^*}{\partial x^*} + v^* \frac{\partial T^*}{\partial y^*} + w^* \frac{\partial T^*}{\partial z^*}\right) = \left(\frac{\partial^2 T^*}{\partial x^{*2}} + \frac{\partial^2 T^*}{\partial y^{*2}} + \frac{\partial^2 T^*}{\partial z^{*2}}\right) + H^* \tag{46}$$

Where Pr corresponds to the Prandtl number mentioned earlier in Equation (22). By removing the turbulent subscripts we can see the ratio that provides a comparison between the molecular and thermal diffusion in:

$$\mathrm{Pr} = \frac{\mu C_p}{k} \tag{47}$$

The product of Reynolds number and Prandtl can also be written as the Peclet number which then relates the rate of advection of a flow to the rate of its diffusion. Scaling the temperature and enthalpy gives:

$$T^* = \frac{T - T_0}{\Delta T} \tag{48}$$

$$H^* = \frac{L^2}{k\Delta T} \tag{49}$$

Where ΔT is the temperature interval. In order for the discretesized values and equations to be applicable, the boundary conditions also need to be dimensionalized. To start with, we will look at equations (35a-c) and discretesize the surface tension gradient which will introduce the dimensionless variable:

$$Ca = \frac{\mu U}{\gamma} \tag{50}$$

This is defined as the Capillary number that gives the ratio between viscous forces versus surface tension. Next, equations (36) and (37) force the heat flux to be dimensionalized by:

$$q^* = \frac{qL}{k\Delta T} \tag{51}$$

And the Stefan-Boltzmann constant in equation (37) to be dimensionalized as:

$$\sigma^* = \frac{\sigma L \Delta T}{k} \tag{52}$$

The remaining variables in equations (30-38), ρ, μ, k, correspond to material properties that are scaled using characteristic reference values similar to the scaling method applied

in equations (39) and (40) while the coefficient of thermal expansion is scaled as:

$$\beta^* = \beta \Delta T \tag{53}$$

And finally the specific heat was scaled slightly different. The value could be scaled similar to the other material properties with a simple characteristic scaling factor, but instead, since the model calls for the property to change as a function of temperature, FIDAP requires it to be scaled as:

$$c_p^* = \frac{H^{**}\mathrm{Pr}}{c_{p0}\Delta T} \tag{54}$$

This allows for the use of an enthalpy model for the variation which takes into account the phase change that occurs during the process. As this is the final remaining variable in the governing equations and boundary conditions, the problem can move onward to the selection of the values for the various quantities.

First, as mentioned previously, the model will use the best known material properties for the Nickel-based superalloy CMSX-4. These values were found through several sources [31-34], some of which were the results of tests performed in the mushy zone temperature realm [31, 34]. This region is of concern as it is found that the material properties change with temperature which is an important fact since the values will drive non-linearity in the heat and fluid flow equations. Since these values were applicable to the region where liquid is present, the material properties were elevated in many cases to account for the region where the material was still solid which helped to create trends that could be used as inputs for the FIDAP code. Material properties that were artificially elevated for this purpose were the surface tension and viscosity. This created a discontinuity at the liquidus line, which appeared around a temperature of 1660K, where the properties were matched to the relationships given in [31-32, 34]. Once the constant physical properties as well as the temperature dependent values were found, the next important step is to choose the scaling factors that would be employed to calculate the results of equations (39-54).

Table 1 – Reference Values for Scaling

Scaling Values	
C_{p0}	0.167 cal/g*K
ρ_0	7.74 g/cm3
k_0	0.079 cal/cm*s*K
ΔT	1000 K
T_0	300 K
L_0	0.01 cm
μ_0	0.1 mPa*s
γ_0	1755 mN/m
U_0	6.1 cm/s

Most of the values were taken directly from the literature as constant values. The only value that needed to be calculated was U_0 which was found by:

$$U_0 = \frac{\alpha}{L_0} \tag{55}$$

Where α is the thermal diffusivity of the material found by:

$$\alpha = \frac{k_0}{\rho c_{p0}} \tag{56}$$

Two of the other values that were did not come directly from literature were the length scale, L_0, and temperature difference, ΔT. These values needed to be chosen appropriately based on established assumptions. First, the basis for the characteristic length can be taken from a study mentioned previously [44] where dimensions of weld pool were on the scale of 0.1-1mm. Therefore, we would not want the characteristic scaling length to be larger than any dimension in the problem. From here, the ΔT value must be chosen. This decision came from the expected temperature difference that would be found along the characteristic length. Taking into account the high energy density of the laser beam, the melting temperature of the material, and the aforementioned weld pool dimensions, the value for ΔT was chosen as 1000 K. This was also found to assist in the convergence behavior of the solution.

Once all of the equations, inputs, and boundary conditions were properly scaled the important assumptions of the actual solution to the problem must be examined. The setup for the problem is clearly outlined in the FIDAP manual [43] as each statement in the input code had several values to choose from. First, we will examine the problem as

a fully three dimensional solution. This is due to the dimensions of the FIDAP mesh which involves a block significantly large enough to allow the heat to dissipate freely without ever reaching the actual boundaries. This can be seen earlier in Figure 10. To reiterate, earlier in the discussion of the governing equations, one of the simplifying assumptions was to solve the problem in a quasi-steady state scenario. This was achieved by creating a translation of the origin in the problem based on the specified travel speed of the heat input. These assumptions apply to the entire problem, but since there is a liquid phase present, many more specifications need to be made. The liquid metal will be treated as an incompressible, Newtonian fluid. As seen in Figure 10, the top surface of the liquid region will be treated as a free surface to allow for the effects of the surface tension gradient which will contribute to the Maragoni convection. A final specification is whether the fluid should be treated as laminar or turbulent. As discussed earlier, studies are divided on which behavior is found in the weld pool. For the current problem, there are no Lorentz forces to create surface instabilities or any other driving force that would suggest that the problem would be turbulent. Taking velocities and dimensions found in the literature [11, 39] and assumptions already stated in the problem statement thus far, the Reynolds number can be found to be on the order of 200 which is far less than any criterion for the transition as stated. This claim will be discussed further in the results portion. In addition to these initial specifications the code employed both relaxation and upwinding schemes in order to assist in the convergence of the solution which was based on specified tolerance values. Upwinding is a method in which the parameters are discretized in order to remove oscillations in the iterations that appear in partial differential equations [43]. Several combinations of coefficients could be used for the relaxation method. As seen in [43] the values could be tailored to the specific problem type. The current problem used slightly elevated values, due to the complexity of the problem and the increased demand for convergence, than were given for laminar flows involving buoyancy.

From Figure 10, the mesh was created with three-dimensional quadratic elements that were denser near and in the liquid region for computation purposes.

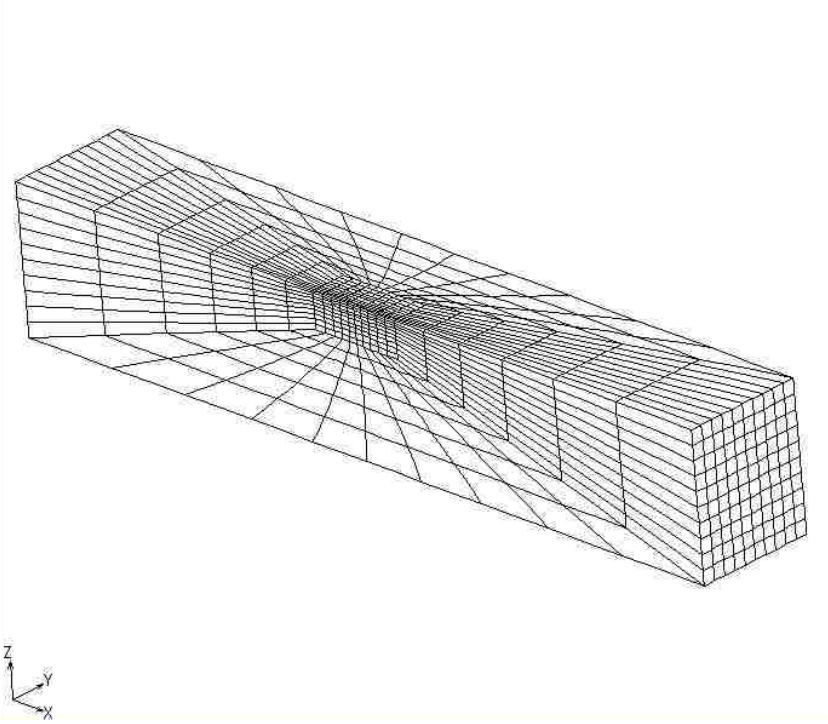

Figure 11 – Computational FIDAP Mesh

As seen in Figure 11, the distance between the edge of the liquid zone and the boundary of the solid portion surrounding it, is sufficient to support the use of the three-dimensional computation. The final values that remain out of the discussion thus far are the values needed for heat input found in Equation (36). For this, the laser efficiency, which is a measure of the amount of energy that is absorbed into the material, of the process was chosen to be 0.5 which was supported by environmental data. This low efficiency value comes from many factors including reflection and other surface based interferences that reduced the amount of absorptivity. Finally, the distribution factor, *f*, was set as 3.0 to properly model the amount of heat at the surface.

Results and Discussion

The above problem statement was calculated for three different sets of parameters in order to view the behavior of the equations and variables. These sets of parameters were based on the assumptions laid out in [11, 37, and 44] with the elevated material constants, as well as the material properties found in [31-34] which gave both constant and temperature dependent values. Two different combinations of velocities and power inputs were used: 350W @ 0.4 cm/s and 450W @ 0.8 cm/s. These values were chosen based on literature findings as well as trial runs of the program performed in order to determine convergence abilities of the codes. With the vast differences in the Heat Input value, Equation (25), the effects of the program's computational techniques can be seen as well as the differences in the assumptions.

Table 2 – Results from Actual Constants Calculations

	Actual Constants			
	350 W 0.4 cm/s		450 W 0.8 cm/s	
	DebRoy's Code	FIDAP	DebRoy's Code	FIDAP
x	1.587 mm	Did not melt	1.752 mm	1.847 mm
y	1.559 mm		1.698 mm	2.121 mm
z	0.189 mm		0.1851 mm	0.035 mm
T_{max}	2232 K	1651 K	2355 K	1684 K
u_{max}	552 cm/s	Did not melt	678 cm/s	41.2 cm/s
v_{max}	613 cm/s		813 cm/s	40.7 cm/s
w_{max}	52 cm/s		59 cm/s	15.1 cm/s

Table 2 shows the comparison of the results obtained from the two different codes where x, y, and z refer to the dimensions in these direction, and u, v, and w refer to velocities in the x, y, and z directions, respectively. In these trials, the material properties were kept constant instead of being temperature dependent, since the FORTRAN code developed by DebRoy et al [26, 44] uses constant property values.

Table 3 – Known Constants used for Table 2 Results

$C_{p\text{-}solid}$	0.195 cl/gm*K
$C_{p\text{-}liquid}$	0.167 cl/gm*K
ρ	7.74 gm/cm^3
k_{solid}	0.068 cal/cm*s*K
k_{liquid}	0.079 cal/cm*s*K
μ	0.1 g/cm*s
$d\gamma/dT$	-1.37 dynes/cm*K

The values shown in Table 3 are the best known constants for the material properties obtained from the literature [32-34]. These calculations were performed as if no prior knowledge of the behavior inside the weld pool was known. This eliminates the need for elevated material constants which are based on the assumption that the fluid in the weld pool is turbulent. The details of such calculation will be discussed next. Returning to the results in Table 2, the first item of note is that the material does not get hot enough to melt in the FIDAP model when the lower power input and slower speed are used. This can be seen in Figure 12 where the isotherm representing the melting temperature, a red line at the normalized value of 1.36, which is equivalent to 1660K as seen in Equation (48), is not present. The other isotherm of importance, at a normalized value of 1.32 or 1620K, represents the solidus line thereby showing the "mushy zone" discussed earlier in the grain orientation section. Since the only value of any pertinent comparison is the temperature, it was found that the value from the Penn State code was around 26% higher than that of FIDAP. The accepted value for finding the percent difference was the DebRoy code since it has been found to be very close to experimental results in [44].

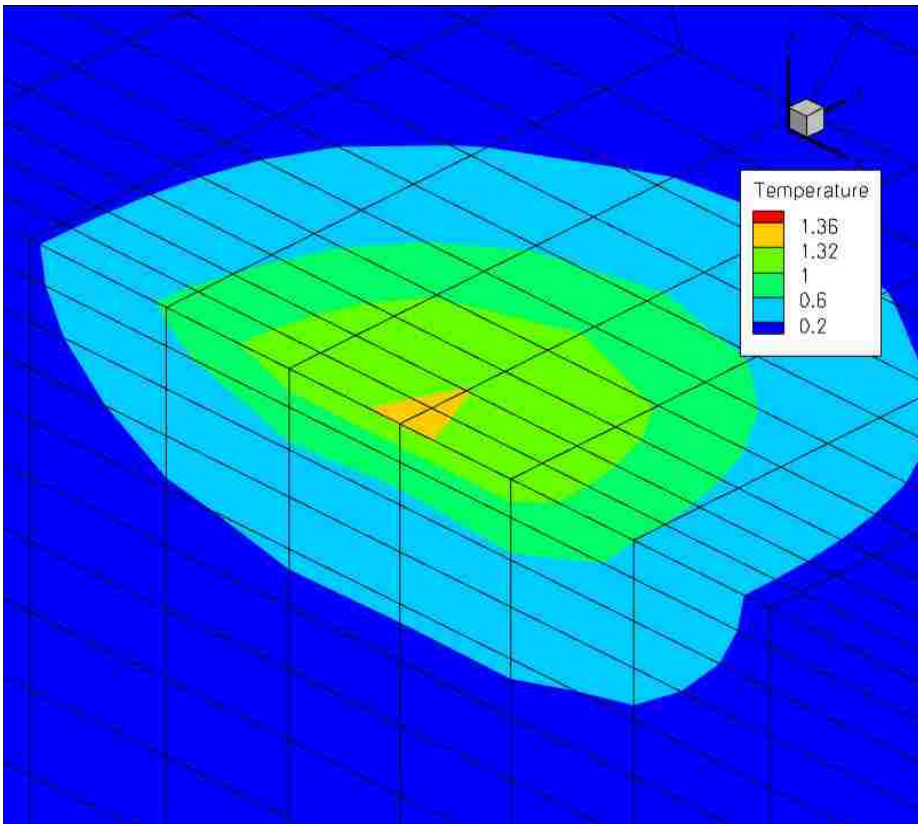

Figure 12 – FIDAP Results for 350W @ 0.4cm/s Known Constants

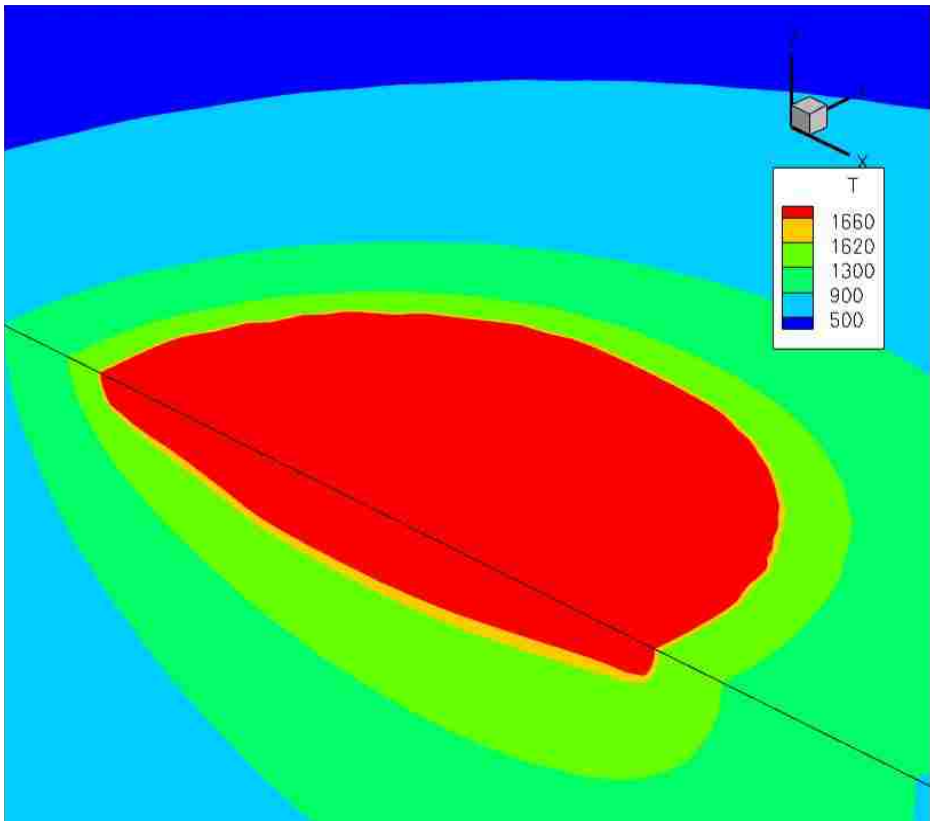

Figure 13 – DebRoy Code Results for 350W @ 0.4cm/s Known Constants

The results from the higher heat input value showed a much closer comparison in some instances as can be seen in Figures 14 and 15. Looking at the dimensions of the weld pool, the lengths of the pools were in close agreement while the widths were slightly further apart at around 25% difference. The remaining dimension in the z-direction was where much of the discrepancy arose in most of the calculations. The FIDAP program did not seem to accurately predict a deep enough weld pool. This leads back to the ideas expressed in the turbulent section where it was stated that the turbulent models actually predict shallower pools than their laminar counterparts. This difference in shape was also shown in Figure 9 in the turbulence section. Obviously this leads to the argument of why the turbulent based elevated values were used at all. Once again the temperatures found by FIDAP were off by a similar margin to the lower heat input problem.

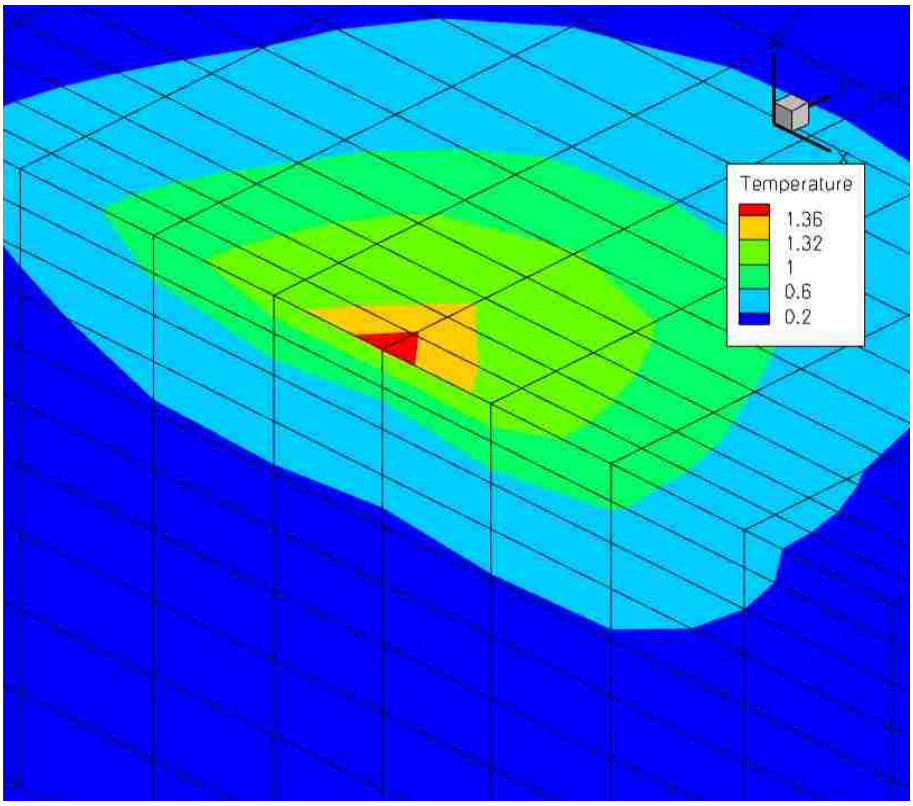

Figure 14 – FIDAP Results for 450W @ 0.8cm/s Known Constants

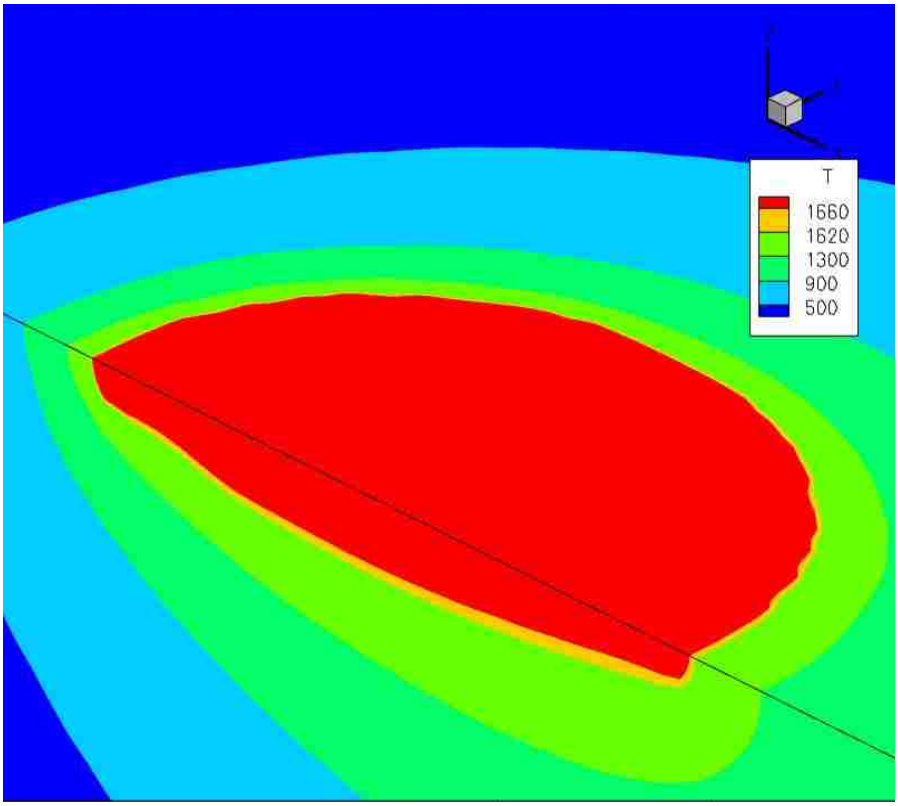

Figure 15 – DebRoy Code Results for 450W @ 0.8cm/s Known Constants

In both cases, the velocities were incredibly high for the DebRoy Code calculations. This is most likely due to the way in which the code was developed. Also mentioned in the turbulent section, Choo and Szekely [37] found that laminar models often predicted larger velocity magnitudes than their turbulent counterparts. The velocity values that were obtained in the FIDAP results were in close agreement with the maximum values found in other studies in the literature [10-11]. This leads to some confusion as to why the codes accurately predict certain characteristic dimensions of the weld pool, but not all.

Table 4 – Results from Turbulent Based Constant Assumption

Elevated Constants				
	350 W 0.4 cm/s		450 W 0.8 cm/s	
	DebRoy's Code	FIDAP	DebRoy's Code	FIDAP
x	1.396 mm	1.219 mm	1.568 mm	5.025 mm
y	1.389 mm	2.486 mm	1.484 mm	5.570 mm
z	0.377 mm	0.176 mm	0.396 mm	0.484 mm
T_{max}	2228 K	1711 K	2365 K	1844 K
u_{max}	28.3 cm/s	6.21 cm/s	34.1 cm/s	16.3 cm/s
v_{max}	29.4 cm/s	9.64 cm/s	35.5 cm/s	17.7 cm/s
w_{max}	9.29 cm/s	5.45 cm/s	10.8 cm/s	12.5 cm/s

Table 4 displays the results from the different codes using constants that were elevated based on an assumption that the fluid would be turbulent in the pool as mentioned in Equations (20-21). These elevated values, which can be found in Table 5, can be compared to those found in Table 3. The only changes occur within the liquidus thermal conductivity and the liquid viscosity.

Table 5 – Elevated Constants used for Table 4 Results

Elevated	
$C_{p\text{-}solid}$	0.195 cl/gm*K
$C_{p\text{-}liquid}$	0.167 cl/gm*K
ρ	7.74 gm/cm^4
k_{solid}	0.068 cal/cm*s*K
k_{liquid}	0.2 cal/cm*s*K
μ	3.0 g/cm*s
$d\gamma/dT$	-1.37 dynes/cm*K

Since the Penn State code was designed to accommodate these types of constants, the velocity magnitudes were much closer to the acceptable value range than those found using the known constants. With the lower heat input calculations, the dimensions of the weld pools were obviously in much closer agreement than those found with the known constants since the melting temperature was never reached as seen in Table 2. Continuing to examine the results in Table 4, the dimensions for the x-direction were in close comparison with around 12% difference found. On the other hand, the dimensions in the y-direction were off by close to 79% difference. This could be attributed to the y-direction component of velocity being 1.5x that of the x-component. And once again, the depth of the weld pool was a considerable amount off at around 53% difference. The appropriate trend was also observed with the decrease in velocity magnitudes in the FIDAP results, although the known constants actually were closer to acceptable values. The final item for comparison was the temperature which was off by around 23% giving way to a somewhat consistent percent difference in the mid-twenty percent range in this category.

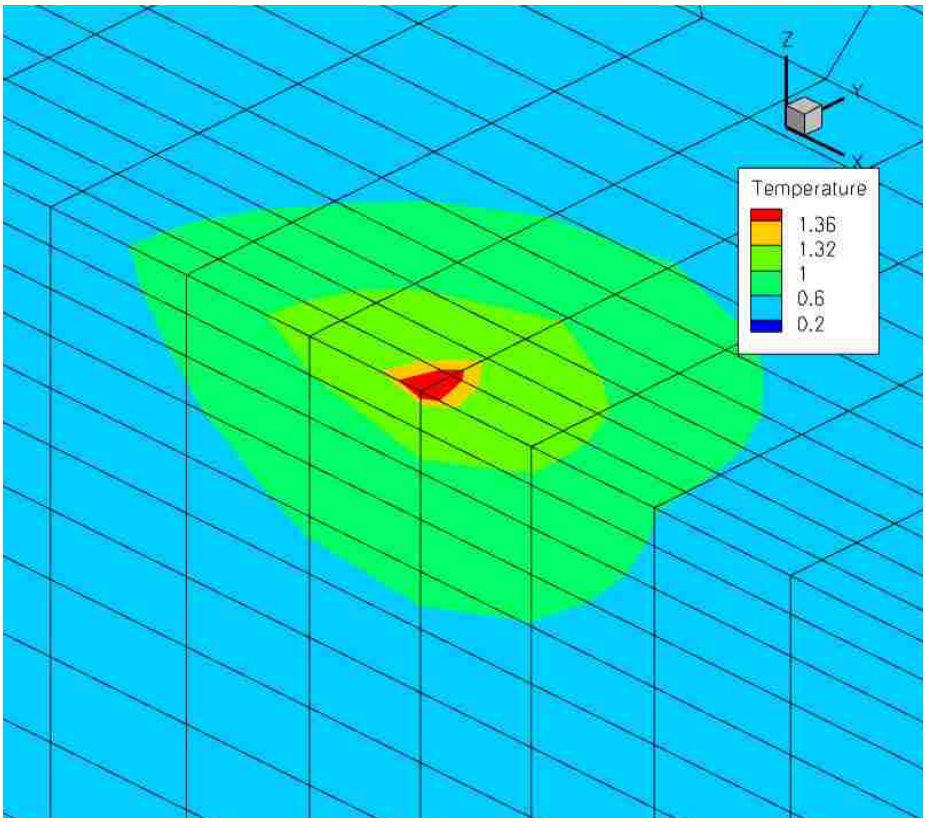

Figure 16 – FIDAP Results for 350W @ 0.4cm/s Elevated Constants

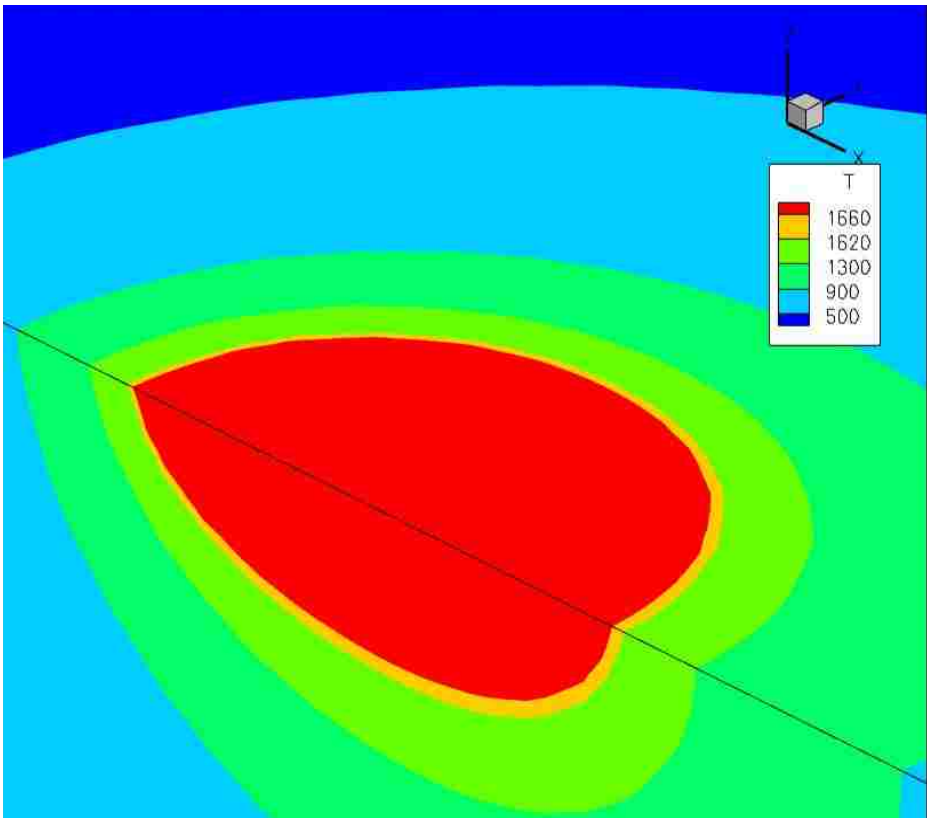

Figure 17 – DebRoy Code Results for 350W @ 0.4cm/s Elevated Constants

As seen above in Figure 16, the pool shape was actually elongated perpendicular to the direction of the moving heat source. This is actually quite opposite of the expected trend.

Once the higher heat input value was used in the FIDAP, a big jump in the dimensions of the weld pool was observed. This jump was actually large enough that the depth of the weld pool was overestimated by the FIDAP program by over 20% as seen in Table 4. Also seen in the results, the x- and y-direction jumps surpassed the FORTRAN results to climb to 2-3 times larger values than the accepted ones. In this case, the depth was actually the closet dimension to the accepted values. These dimensions, seen in Figure 18, returned to a more circular shape than the previous results in Figure 16. Another comment on the pool shapes is the comparative sizes of the "mushy zones" as defined by the second highest isotherms in each figure. The FIDAP code predicts much larger zones than the FORTRAN code which should be avoided as discussed in the grain orientation section. Although the velocities took a significant plunge, the values were still on the same order of magnitude as the FORTRAN results.

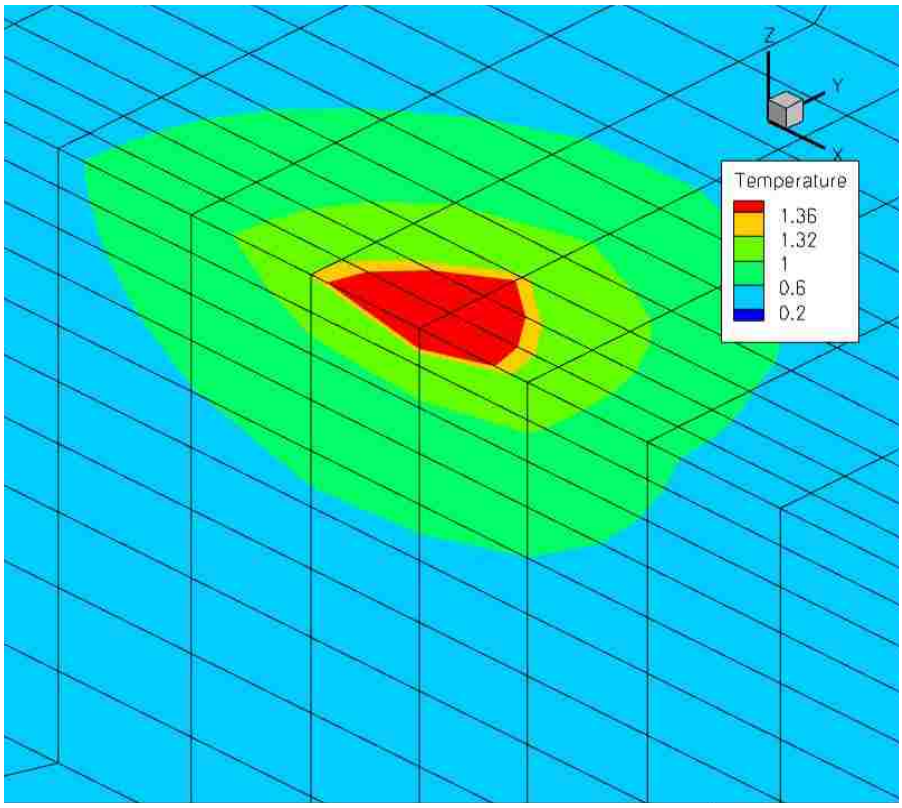

Figure 18 – FIDAP Results for 450W @ 0.8cm/s Elevated Constants

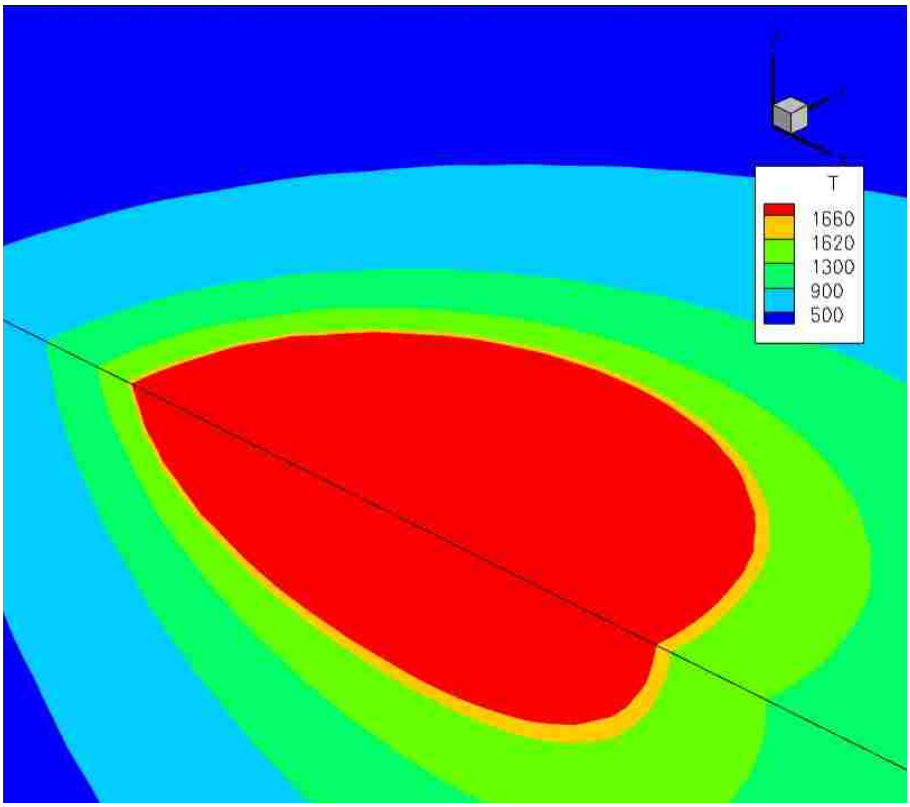

Figure 19 – DebRoy Code Results for 450W @ 0.8cm/s Elevated Constants

The final round of calculations that were performed used the best known values for the material properties. This took into account temperature dependent properties, which are considered to be the most accurate, although the most resource consuming. These could only be performed in FIDAP since, as mentioned earlier; the edition of the FORTRAN code that was used was not built to handle such inputs. During these calculations, a four-point curve is employed for each of the temperature dependent material properties which are defined as such only in the liquid realm. The surface tension points were created in order to keep the $\partial\gamma/\partial T$ value similar to the values shown in Tables 3 and 5 while the viscosity equation used elevated values below the liquidus temperature in order to account for the phase transition of the material. Some issues arose when exploring the values for this property though. Sources in the literature [32, 34] report their results that were found only in the regions from near the melting temperature up to around 1800K. As seen in the previous results in Tables 2 and 4, temperatures can reach much higher values than that. With the small magnitude of the property it was, for all practical purposes, kept constant once the melting temperature had been reached. All of this information can be seen in the appendix section.

Since the FORTRAN code was not designed to handle temperature dependent properties, the most suitable set of data to use for comparison would be those found using the elevated constants.

Table 6 – Results from "Best" Calculations

"Best" Values				
	350 W 0.4 cm/s		450 W 0.8 cm/s	
	DebRoy's Code	FIDAP	DebRoy's Code	FIDAP
x	1.396 mm	8.019 mm	1.568 mm	8.898 mm
y	1.389 mm	7.982 mm	1.484 mm	8.818 mm
z	0.377 mm	1.409 mm	0.396 mm	1.612mm
T_{max}	2228 K	2599 K	2365 K	2967 K
u_{max}	28.3 cm/s	2.79 cm/s	34.1 cm/s	14.2 cm/s
v_{max}	29.4 cm/s	2.74 cm/s	35.5 cm/s	6.81 cm/s
w_{max}	9.29 cm/s	2.65 cm/s	10.8 cm/s	5.02 cm/s

From Table 6, it can easily be seen, that with the best known values for the material properties, something is still missing in the FIDAP calculation. Although it is good that the temperatures are higher than they have been in the previous calculations, it leads to

weld pool dimensions that are far too high to be acceptable. Reasons for this could be the aforementioned issue with the material properties. Since the values for the material properties could only be found as linear models up to around 1800K, the behaviors above this line are unknown. The velocity magnitudes on the other hand dropped a bit so that they are no longer on the same order as the accepted values as they were in the results found in Table 4.

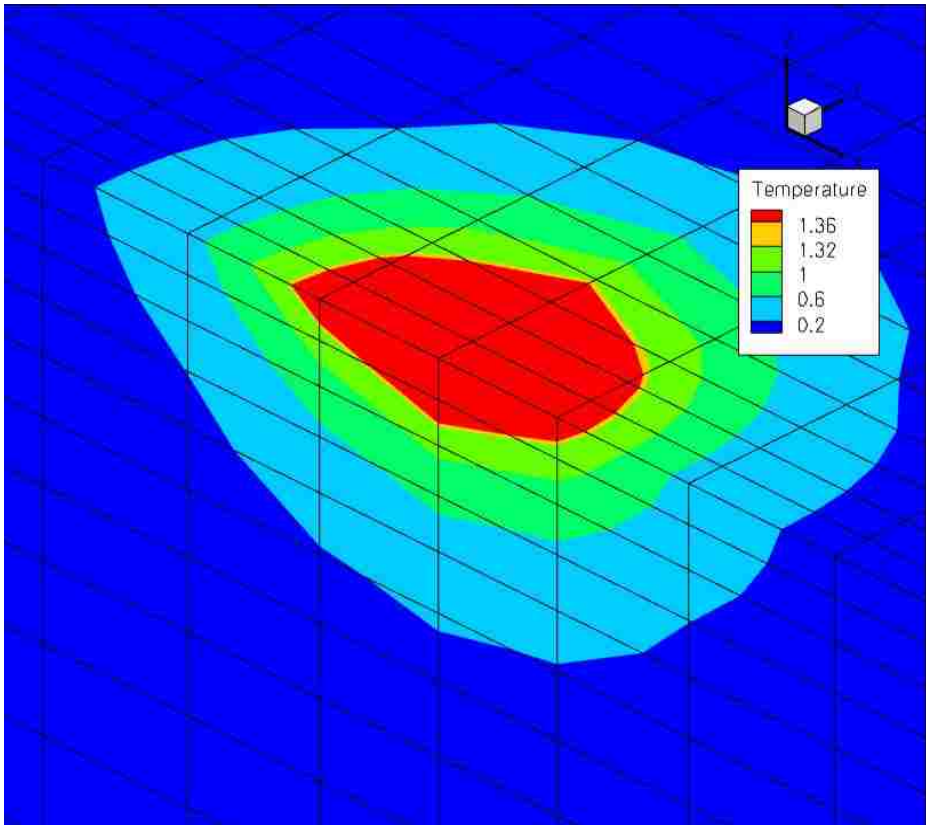

Figure 20 – FIDAP Results for 350W @ 0.4cm/s Best Values

As seen in Figure 20, one good thing that came as a result of these calculations was a reduced "mushy zone" size. This is great news as it is one of the main reasons for creating such a model as discussed earlier in the grain orientation section. This same trend can also be seen in the higher heat input value results in Figure 21. Also seen in both figures, is a shape that is close to circular, but slightly elongated in the proper direction. This shows that although the magnitudes are much too great, the overall prediction capabilities are getting closer.

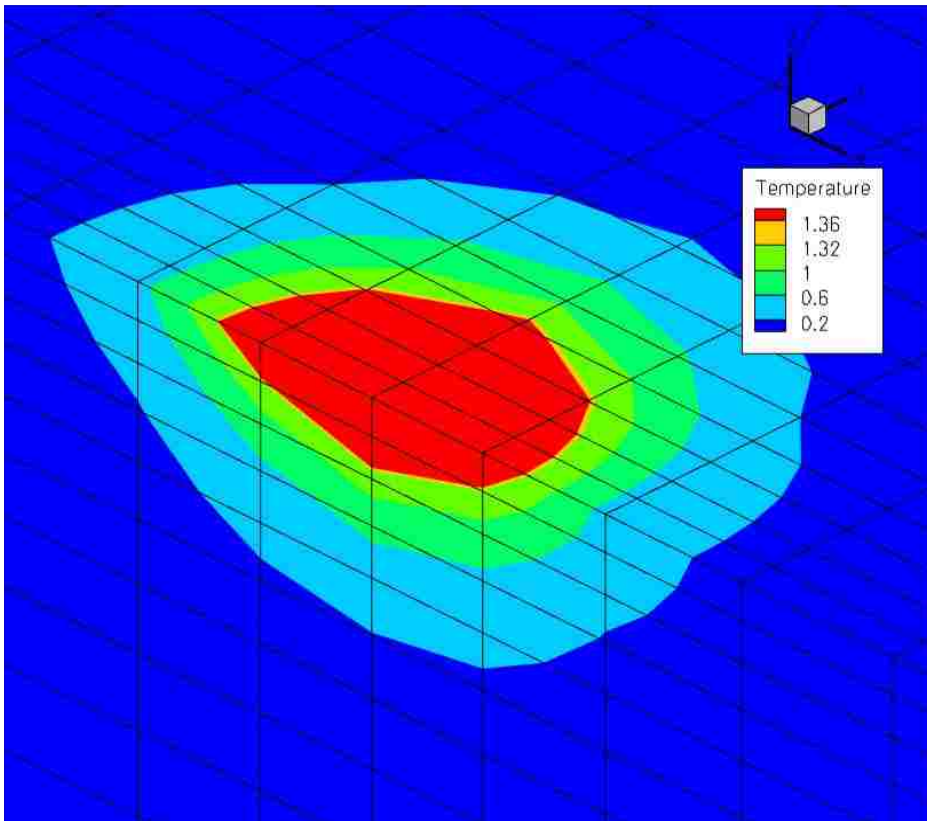

Figure 21 – FIDAP Results for 450W @ 0.8cm/s Best Values

But these results still lead to a puzzling discovery. Although the depths of the weld pools are now being predicted, and even overestimated in certain instances, the shape of the pool stays as a shallower version of the accepted pool shape. By this it is meant that the x- and y-direction dimensions are consistently much higher than the z-direction value. To quantify this, the FORTRAN results from the elevated constants show the x- and y-direction dimensions to be slightly greater than 3x larger than the z-direction values while the same ratios in the FIDAP calculations were in the double digit range.

There are several possibilities that could help the model become more accurate. The first is to use a slightly different heat input model. Instead of using a Gaussian distribution, as many other models use, perhaps a model that is closer to a double ellipsoid. With this type of model the heat would be entering from within the depths of the work piece, possibly taking into account the beginnings of a keyhole weld or other depressions that are caused by the extreme energy input. It has been established earlier that the laser beam is closest to the Gaussian distribution, but a possibility of adding a second Gaussian curve, inverted and into the depth of the material, could accommodate

this idea. Figure 22 shows an edited version of Figure 5 in attempts to portray this theory. This type of model could help the prediction of the depths of the weld pools. For now, the creation of a new heat input this complex was beyond the scope of the current work but will be explored in the future.

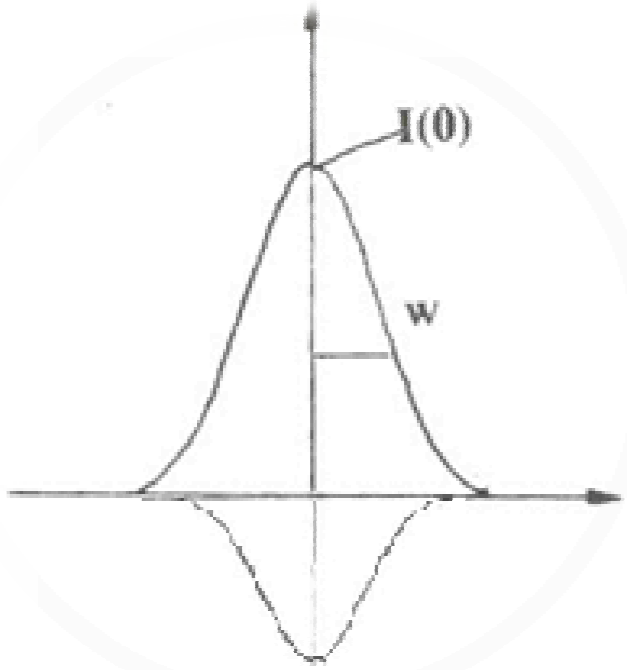

Figure 22 – Double Gaussian Heat Input

Instead of using a double Gaussian input as seen in Figure 22, a conical, linear type of heat flux was used for the input into the depth of the material. This came as a result of the constraints the FIDAP program has on the flux boundary conditions. Therefore in order to put the heat into the depth, point sources at specified nodes were used as the other methods that could be used would either be too complex or conflict with previous arguments in the code. As an example, the heat input at the node below the origin on the opposite element face as seen in Figure 23, was set to the maximum value of the Gaussian distribution. This value was arrived upon by solving Equation (36) at the origin and assuming this heat value would carry through. From here the nodes in the closet proximity to this were given flux values of 1/2 the maximum value of the Gaussian distribution. This was done in hopes of creating a simple linear relationship. Nodes outside of this range were not given additional values as it would seem that the heat into the depth would not affect a large area.

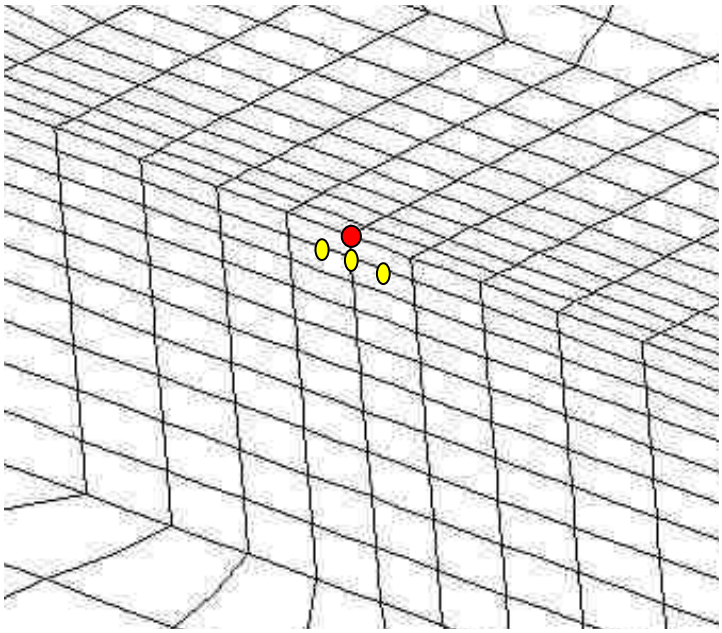

Figure 23 - Nodes for Additional Heat Input

The larger red point refers to the origin while the 3 smaller, yellow points refer to the nodes where the heat input conditions were applied for the depth. A fourth point was also used at x=0 and the same z-coordinates as the other three.

As discussed earlier, it was never clear why the DebRoy calculation used the elevated material constants. This being said, the calculations performed to examine the effects of heat flux into the depth of the material only used the best known values and the actual constants.

Table 7 - Results from Into the Depth Calculations

	Into Depth Heat Input			
	350 W 0.4 cm/s		450 W 0.8 cm/s	
	Best Known	Actual Constants	Best Known	Actual Constants
x	8.028 mm	Did not melt	10.42 mm	1.229 mm
y	7.977 mm		10.25mm	1.639 mm
z	1.414 mm		2.383 mm	0.031 mm
T_{max}	2599 K	1653 K	3369 K	1678 K
u_{max}	2.79 cm/s	Did not melt	16.01 cm/s	40.1 cm/s
v_{max}	2.73 cm/s		15.43 cm/s	40.4 cm/s
w_{max}	2.65 cm/s		6.48 cm/s	14.9 cm/s

Table 7 contains some interesting results. The first being that even with increased heat inputs, the material still did not reach the melting temperature with the lower heat inputs

and actual material constants. This is important to note as it shows that the material properties have a more important impact than other parameters in some instances. Next, compared to the values found in Table 6, the lower heat input value with the best known properties was barely affected by this change. This could reinforce the idea regarding how important the heat transfer due to the surface tension is since the original heat input at the surface overpowers the additional sources in the depth. In conjunction with this, the observation also shows that the theories regarding the velocities in the pools are also valid which say that swirling effects of within the pool are strongest on the outer edges and surfaces. Therefore, with the low velocities in the regions in the depths of the material, it makes sense that the additional sources had little impact to this point.

Next, the calculation performed using the higher heat input value and actual constants for some reason resulted in a smaller weld pool with slightly lower maximum temperatures and velocities. This again can be attributed to the idea stated above in that the surface heat flux overpowers the other sources. This is important in the current case as the additional sources would actually occur at points much lower than the initially calculated pool depth.

Finally, the calculation performed with the heat input value and best known material properties kicked the previous trends and actually was found to have around a 15% increase in the values of the x- and y-direction dimensions of the pool as well as the maximum temperature found while the depth actually increased by almost 50%. Since this calculation was found to be more affected by the additional heat sources it is important to examine why this would have occurred. The first possible explanation is that the magnitude of the additional heat sources is much higher since it is based on the initial heat input at the surface. The correlation cannot be continued though for the reasons mentioned above regarding the high heat input with the actual constants calculation. Also, the additional heat sources would occur well within the limits of the original weld pool depth (as seen in Table 6). This would allow the energy to possibly be distributed more easily with the higher velocity magnitude which goes along with the ideas stated in discussion of the lower heat input with the best known properties calculation.

Upon reviewing the results from the various calculations, it is difficult to distinguish what is missing from the FIDAP calculations in order to make a robust model that needs

very few inputs. With the lack of weld pool depth in the FIDAP models, the idea of taking turbulence into account does not seem as though it would help the situation, but instead only take up valuable computer resources in order to solve the highly non-linear problem. As seen in the set of results found in Table 6, the "Best" values for the material properties were indeed properly named as the shape of the pools were closer to being on target, although there was some property that allowed for increased heat transfer which resulted in the pool being much larger than it should be. The known constant values also gave results closer to the expected shape than the elevated constants did. A possible reason for this corresponds to the reason given for the FORTRAN results to be a considerable amount off while using the best known constants; the code was not designed to handle such inputs. Within the FIDAP system, there are sets of parameters for which to solve turbulent problems, but many values must be known depending on the model type used, as discussed in the turbulence section. Since very little is known about the turbulent behavior of metal in the liquid state, many of these required questions cannot be answered. Also, since the goal is to make a robust model that would require very few assumptions, this type of inherent calculation will be avoided.

Other items that could help the prediction capabilities of the model include the material property values. As mentioned in the above, several of the temperature dependent variables were not known for temperatures above 1800K. This is a cause for concern since, as seen previously, temperatures can easily exceed this limitation which could result in unknown phenomena that could have drastic impacts on the fluid flow and behavior in the pool. Unknown behaviors, such as secondary flows, are also difficult to track in the molten metal and very well could be present. As discussed earlier, these types of flows do not necessarily appear in turbulent conditions alone. But in order to study the effects of such flow patterns, some sort of property would have to be implemented in order to force these flows while not affecting other actions in the pool. Again, this theory could be examined more thoroughly in future works.

One final suggestion for future studies is the implementation of the mass flux found in powder deposition. This could be the missing link in the overall solution as the momentum and energy could allow for the depth in the models to grow. Complexities will grow however since the additional mass in the problem will also affect the heat input

efficiency since the particles will absorb some of the laser's energy. This idea also brings up the point that the particle temperature will vary from that of the base material which will create issues with initial temperatures as well as heat flux. A problem involving all of these ideas should give a very accurate model of the weld pool. Whether it all can be incorporated in one nice package is an excellent goal for the road ahead.

Conclusion

It is a difficult task to take into account all of the small variables that can appear in the fluid flow problem in order to develop a robust three dimensional model. If this task can indeed be accomplished without using elevated values, then the ability to predict the weld pool shape and size as well as fluid flow behaviors will be an invaluable asset in the future as turbines play a more important role in the harnessing and distribution of energy and power. This paper has outlined the myriad of different modeling options that can be employed as well as the results of a few such methods. As this work moves forward, the complexity and intricacies will grow at an incredible rate and thus the computer power and resources must grow along with them.

References

[1] N.K. Arakere, G. Swanson, 2002, "Effect of Crystal Orientation on Fatigue Failure of Single Crystal Nickel Base Turbine Blade Superalloys," J. of Eng. for Gas Turbines and Power **124**, pp161-176.

[2] "Power Industry Experiences Surge in Welding Research," Welding Journal **82**, pp40-43

[3] M.B. Henderson, et al., 2004, "Nickel Based Superalloy Welding Practices for Industrial Gas Turbine Applications," Science and Technology of Welding and Joining **9**, pp13-21.

[4] R. Nützel, et al., 2008, "Damage Evolution During Thermomechanical Fatigue of a Coated Monocrsystalline Nickel-base Superalloy," International Journal of Fatigue **30**, pp313-317.

[5] J.M. Gallardo, et al., 2002 "Failure of Gas Turbine Blades," Wear **252**, pp264-268.

[6] H.M. Tawancy, L. Al-Hdhrami, 2008, "Degradation of Turbine Blades and Vanes by Overheating in a Power Station," Engineering Failure Analysis **16**, pp273-280.

[7] D. Nowell, et al., 2003, "Prediction of Fatigue Performance in Gas Turbine Blades After Foreign Object Damage," International Journal of Fatigue **25**, pp939-969.

[8] H.M. Tawancy, L. Al-Hdhrami, 2008, "Failure of Refurbished Turbine Blades in a Power Station by Improper Heat Treatment," Engineering Failure Analysis (2008).

[9] D. Dye, et al., 2001, "Numerical Analysis of the Weldability of Superalloys," Acta Materialia **49**, pp683-697.

[10] W. Duley, 1999, *Laser Welding*, John Wiley & Sons, Inc., New York, NY.

[11] S. Kou, 2003, *Welding Metallurgy: 2nd Edition*, John Wiley & Sons, Inc., Hoboken, NJ.

[12] G.K. Lewis and E. Schlienge, 2000, "Practical Considerations and Capabilities for Laser Assisted Direct Metal Deposition," Materials and Design **21**, pp417-423.

[13] L. Wang, et al., 2008, "Residual Stresses in LENS-Deposited AISI 410 Stainless Steel Plate," *2008 TMS Annual Meeting & Exhibition, Symp. on Neutron and X-Ray Studies for Probing Materials Behavior*, New Orleans, LA.

[14] L. Wang, et al., 2007, "Optimization of the LENS Process for Steady Molten Pool Size," Materials Science and Engineering A **474**, pp148-156.

[15] L. Wang and S. Felicelli, 2007, "Influence of Process Parameters on the Phase Transformation and Consequent Hardness Induced by the LENS Process," Materials Process Fundamentals, TMS. Pp63-72.

[16] J.W. Park, et al., 2003, "Thermo-Mechanical-Metallurgical Modeling of Cracking in Single Crystal Nickel-Base Superalloy Welds," *American Welding Society Conference*, Dallas, TX.

[17] S.A. Tsirkas, et al., 2003, "Numerical Simulation of the Laser Welding Process in Butt-Joint Specimens," J. of Materials Processing Technology **134**, pp59-69.

[18] L. Wang and S. Felicelli, 2006, "Analysis of Thermal Phenomena in LENS Deposition," Materials Science and Engineering A **435-436**, pp625-531.

[19] R. Ye, et al., 2006, "Numerical Modeling of the Thermal Behavior During the LENS Process," Materials Science and Engineering A **428**, pp47-53.

[20] S. Bontha, et al., 2006, "Thermal Process Maps for Predicting Solidification Microstructure in Laser Fabrication of Thin-Wall Structures," J. of Materials Processing Technology **178**, pp135-142.

[21] D. Gery, et al., (2005) "Effects of Welding Speed, Energy Input and Heat Source Distribution on Temperature Variations in Butt Joint Welding," J. of Materials Processing Technology **167**, pp393-401.
[22] H. Wang, et al., 2007, "Effect of Pressure Gradient Driven Convection in the Molten Pool During the Deep Penetration Laser Welding," J. of Materials Processing Technology **184**, pp386-392
[23] C.K. Hsieh, 1994, "Exact Solutions of Stefan Problems for a Heat Front Moving at Constant Velocity in a Quasi-Steady State," International J. of Heat & Mass Transfer **38**, pp71-79.
[24] K.I. Schwendner, et al., 2001, "Direct Laser Deposition of Alloys from Elemental Powder Blends," Scripta Materialia **45**, pp1123-1129.
[25] D.F. Susan, et al., 2006, "Quantitative Characterization of Porosity in Stainless Steel LENS Powders and Deposits," Materials Characterization **57**, pp36-43.
[26] T. DebRoy, et al., 2004, "Heat and Fluid Flow in Complex Joints During Gas Metal Arc Welding-Part I: Numerical Model of Fillet Welding." J. of Applied Physics **95**, pp5210-5219.
[27] J.K. Vitek, et al., 2005, "Welding of Single-Crystal Nickel-Based Superalloys: How to Avoid Stay Grains and Why," *Proc. of 7th International Conf. on Trends in Welding Research,* Pine Mountain, GA.
[28] M. Gäumann, et al., 2001, "Single-Crystal Laser Deposition of Superalloys: Processing-Microstructure Maps," Acta mater. **49**, pp1051-1062.
[29] V. Sass, et al., 1996, "Creep Anisotropy in the Monocrsystalline Nickel-Based Superalloy CMSX-4," *Proc. of 8th International Symposium on Superalloys,* Champion, PA.
[30] Y. Kando, et al., "Effect of Morphology of g' Phase on Creep Resistance of Single Crystal Nickel-Based Superalloy, CMSX-4," *Proc. of 8th International Symposium on Superalloys,* Champion, PA.
[31] Z. Li, et al., 2005, "Measurement of the Density and Surface Tension of Ni-Based Superalloys in the Liquid and Mushy States," Metallurgial and Materials Transactions **36B**, pp247-254.
[32] E. Ricci, et al., 2007, "Density, Surface Tension, and Viscosity of CMSX-4 Superalloy," International J. of Thermophysics **28**, pp1304-1321.
[33] C-M Group Website. http://www.c-mgroup.com/spec_sheets/CMSX_4.htm
[34] K. Higuchi, et al., 2007, "Surface Tension and Viscosity of the Ni-based Superalloy CMSX-4...," Advanced Engineering Materials **9**, No. 5, pp349-354.
[35] N. Charkraborty, et al., 2004, "Three-Dimensional Modeling of Turbulent Weld Pool Convection in GTAW Process," Numerical Heat Transfer, Part A: Applications, **45**, pp391-413.
[36] D.R. Atthey, 1979, "A Mathematical Model for Fluid Flow in a Weld Pool at High Currents," J. of Fluid Mechanics, **98**, pp787-801.
[37] R.T.C Choo and J. Szekely, 1994, "The Possible Role of Turbulence in GTA Weld Pool Behavior," J. of Welding, **73**, pp25-31.
[38] Zhou P., et al., 2004, "Effect of Electromagnetic Force on Turbulent Flow..." J. Central South University of Technology, **11**, No. 3, pp265-269.
[39] Huan Qi, et al., 2006, "Numerical Simulation of Heat Transfer and Fluid Flow in Coaxial Laser Cladding Process for Direct Metal Deposition," J. Applied Physics, **100**

[40] R.W. Messler, Jr., 1999 *Principles of Welding: Processes, Physics,Chemistry, and Metallury,* John Wiley & Sons, Inc., New York, NY.
[41] G.R. Tallback, et al., 2004, "Influence of Model Parameters on 3-D Turbulent Flow..." IEEE Transactions on Magnetics, **40**, No. 2, pp597-600.
[42] A. Mahrle, et al., 2000, "Influence of Marangoni Convection on Weld Pool Shape..." *Proc. of 3rd European Thermal Sciences,* Heidelberg, Germany.
[43] *FIDAP 8 Tutorial Manual,* 1998, Fluent. Inc
[44] T.D. Anderson, et al., 2008, "Stray Grain Formation in Welds of Single Crystal Ni-base Superalloy CMSX-4," PhD Thesis, Lehigh University, Bethlehem, PA.
[45] B. K. Muite, 2003, "The Secondary Flow in a Short Aspect Ratio Circular Lid Driven Cavity at Small but Finite Reynolds Number," PhD Thesis, Princeton University, Princeton, NJ.

Input code with references for explanation. Modeling commands removed for simplicity.

```
FI-GEN
(ELEMENT=1,POINT=1,CURVE=1,SURFACE=1,NODE=0,MEDGE=1,MLOOP=1,MFACE=1,BEDGE=1,S
PAVE=1,MSHELL=1,MSOLID=1,COORDINATE=1)

/ALL DEFAULT VALUES

/Modeling Commands would be located here

FIPREP
 PROB (3-D, INCO, STEA, LAMI, NONL, NEWT, MOME, ENER, FREE, NOST, NORE, SING)

SOLUTION(SEGR=2000,CGS=2000,CR=2000,NCGCONV=0.001,SCGCONV=0.001,velconv=0.001
)

/2000  # iterations used, 0.001 = tolerance levels

 OPTIONS(UPWINDING)
 UPWINDING(HYBRID)
 PRESSURE(MIXED=1.E-8,DISC)
 RELAXATION
/ux  uy   uz   Pres  T  Sur
/0.85 0.85 0.85 0.85 0.85 0
/default values for laminar flow
 0.3 0.3 0.3 0.6 0.3 0.5


/Values for laser beam - can compare/contrast to input.txt value for Debroy,
etc...

/parameters for reference values----------------------------
/power (watts)
 $pw=500
/welding velocity(cm/sec)
 $v=0.585
/efficiency
 $eff=0.55
/joule to cal conversion factor
 $jtocal=0.239
/laser radius
 $rb0=0.075
/specific heat
 $cp0=0.167
/density
 $rho=7.74
/conductivity
 $k0=0.079
/temperature interval
 $dt=1000
/base temp (K)
 $t0=300
/characteristic length
 $l0=0.01
/thermal diffusivity
 $alpha=$k0/($rho*$cp0)
```

```
/velocity
 $u0=$alpha/$l0
/ $u0=10
/gravitational acceleration
 $g=981
/viscosity
 $mu0=0.1
/surface tension
 $gamma0=1755
/dimensionless heat source flux through free surface
 $fp=$pw*$jtocal*$eff/($k0*$dt*$l0)
/dimensionless laser diameter
 $rb=$rb0/$l0
/stefan boltzman constant
 $st=5.67E-12
/dimensionless stefan boltzman
 $stndim=$st*$jtocal*$l0*$dt*$dt*$dt/$k0

/parameters for dimensionless numbers-----------------------
/prandtl
 $PR=$mu0*$cp0/$k0
/reynolds
 $RE=$rho*$u0*$l0/$mu0
/capillary
 $beta=1
 $CA=$beta*$mu0*$u0/$gamma0
/Froude
 $FR=$u0*$u0/($g*$l0)

 EXEC (NEWJ)
 DATA(CONT)

/Names come from above @mshell commands, etc

 ENTI (NAME = "liquid", FLUID,MDENS=1,MCOND=1,MVISC=1,MSPHT=1,MSURF=1)
 ENTI (NAME = "solid", SOLID,MSPHT=2,MCOND=2,MDENS=2)
 ENTI (NAME = "radiation", PLOT)
 ENTI (NAME = "radiation2", RADIATION,BLACK,MEMSV=2)
 ENTI (NAME = "symmetry", PLOT)
 ENTI (NAME = "freesurface", SURF,DEPTH=0)

/solid properties-------------------------------
 DENS (SET=2,CONS = $RE)
 COND (SET = 2, CONS = (0.068/$k0))
 SPEC (SET=2,CONS = ($PR*0.195/$cp0))
 EMISSIVITY(SET=2,CONS=1,STEFB=$stndim,REFTEMP=((300-$t0)/$dt))

/values come from table that uses non-dimensional inputs for various
parameters
/Density, conductivity, spec heat, emmisivity

/liquid properties-------------------------------
 DENS (SET=1,CONS = $RE)
 /COND (SET = 1, CONS = (0.079/$k0))
 COND (SET=1,CURVE=4)
 ((-1000-$t0)/$dt) ((1620-$t0)/$dt) ((1660-$t0)/$dt) ((10000-$t0)/$dt)
 (0.06/$k0) (0.068/$k0) (0.079/$k0) (0.095/$k0)
```

```
 /SPEC (SET=1,CONS = $PR)
 SPEC (SET=1,ENTHALPY= 4,SPATIAL)
 ((-1000-$t0)/$dt) ((1620-$t0)/$dt) ((1660-$t0)/$dt) ((10000-$t0)/$dt)
 ((45*$PR)/($cp0*$dt)) ((48*$PR)/($cp0*$dt)) ((60*$PR)/($cp0*$dt))
((70*$PR)/($cp0*$dt))
 /VISC (SET=1,CONS=0.1/$mu0)
 VISC (SET=1,CURVE=4)
 ((-1000-$t0)/$dt) ((1600-$t0)/$dt) ((1660-$t0)/$dt) ((10000-$t0)/$dt)
 (3100/$mu0) (3000/$mu0) (0.1/$mu0) (0.1/$mu0)
 /SURFACETENSION(SET=1,CONS=(1755/($CA*$gamma0)))
 SURFACETENSION(SET=1,CURVE=4)
 ((-1000-$t0)/$dt) ((1620-$t0)/$dt) ((1840-$t0)/$dt) ((10000-$t0)/$dt)
 (1885/($CA*$gamma0)) (1885/($CA*$gamma0)) (1755/($CA*$gamma0)) (-
4200/($CA*$gamma0))
/ VOLUMEXPANSION(SET=1,CONSTANT=(0.0001*$dt))
/-------------------------------------------------

/curve - y vs x (var vs Temp)

GRAVITY(MAGNITUDE=(1/$FR))
/from nondim table

/coordinate for the heat source location(in the middle of free surface)
 COORDINATE(ADD,SYSTEM=2,ROTATION,CARTESIAN)
 0 0 0

/boundary conditions-----------------------------------
 BCFL (HEAT, ENTI = "freesurface", SUBR=2,SYSTEM=2,CART)
 $fp $rb
/???

 BCFL (HEAT, ENTI = "symmetry", CONS=0)
/symmetrical bc
 BCNODE(TEMP, ENTI = "radiation", CONS = ((300-$t0)/$dt))
/surface temp for radiation area
 TRANSLATION(UX=($v/$u0))
 BCNODE(UY,ENTI="symmetry",ZERO)
 BCNODE(SURF, ENTI = "freesurface",ZERO)
 BCNODE(UZ, ENTI = "freesurface",ZERO)
/velocity bc's & keep surface constant
END
 CREATE(FIPREP,DELE)
 CREATE(FISOLV)
```

Vita

Jeremy Payne is originally from Portville, NY where he graduated from Portville Central School. He is the son of Wendy Eaton and Jeffrey Payne and the stepson of John Eaton. Jeremy attended Youngstown State University in Youngstown, OH where he obtained a Bachelors of Engineering degree in Mechanical Engineering as a member of Youngstown State's University Scholars program. Also while at Youngstown, Jeremy worked for General Electric's Ohio Lamp Plant in Warren, OH. Jeremy was also very active in his fraternity Sigma Tau Gamma. Following graduation from Youngstown, he attended Lehigh University for his graduate studies. After completion of the Master of Science degree, Jeremy plans to continue his studies at Lehigh University in hopes of earning a PhD in Mechanical Engineering.